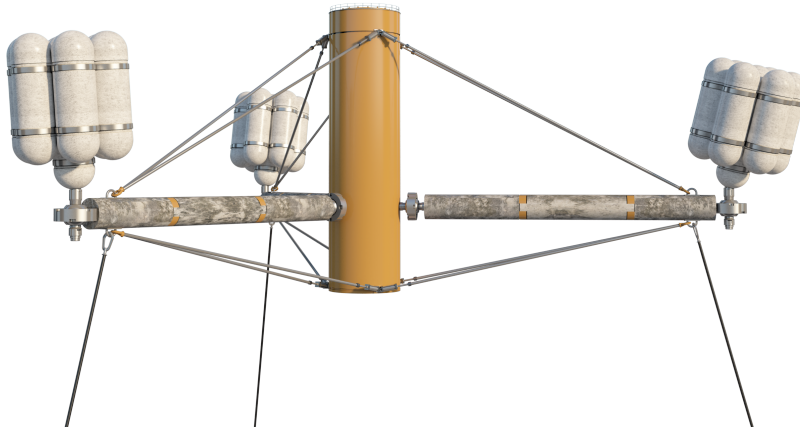Graphical Abstract

An Innovative Second-Order Design Method for the Structural Optimization of the Spider-FLOAT Offshore Wind Platform

Rick Damiani,Max Franchi

Highlights

An Innovative Second-Order Design Method for the Structural Optimization of the Spider-FLOAT Offshore Wind Platform

Rick Damiani,Max Franchi

- SpiderFLOAT Offshore Floater Tool for Sizing (SOFT4S), An innovative model for the design of the Spider-FLOAT platform for floating offshore wind turbines

- 2nd order beam theory extension accounts for buckling and shortening due to bending in the main leg

- Full serviceability limit state (SLS) and ultimate limit state (ULS) design steps identified for dimensioning the SpiderFLOAT leg, a prestressed concrete beam

- The new analytical method allows for the SpiderFLOAT cable and leg optimization and for the identification of margins from cable-slack conditions

- Prestressing loads dominate over hydrodynamic loads

An Innovative Second-Order Design Method for the Structural Optimization of the SpiderFLOAT Offshore Wind Platform⋆

Dr. Rick Damiani^{a,*} (Principal Engineer), Max Franchi^{a} (Principal Engineer)

^{a}*The Floating Wind Technology Company, 18960 W 92nd Dr., Arvada, CO 80007, USA*

ARTICLE INFO

ABSTRACT

The SpiderFLOAT (SF) is an offshore wind turbine substructure that promises to drastically reduce project capital expenditure via its modularized slender structure, efficient load path, and effective use of materials. The structural design of the SF must both guarantee component reliability as well as floater stability. This article discusses the theory and the analytically developed method to determine the internal loads and the required dimensions of the SF's main components during preliminary design. The classic elastic beam theory is extended to a higher order to account for buckling risk and shortening due to bending, and applied to the SF's typical leg member. Two key load cases are considered in this preliminary sizing, analyzed against both service and ultimate limit states (SLS and ULS). The first loading scenario occurs on a dry-dock during SF's assembly and is associated with the pretensioning of the cables, which guarantee both the overall structure stiffness as well as the concrete leg and stem prestress. The second load case is an operational condition at sea and near turbine rated-power. After assessing the loads, the leg dimensions and the reinforcement geometry are determined by satisfying both SLS and ULS requirements based on design standards. The newly developed structural model is implemented in the software tool SOFT4S which was verified against ANSYS. The excellent agreement between the two codes proved that the computationally light SOFT4S can be reliably used in the optimization of the SF components in the context of control co-design, where both controls and structures are simultaneously designed to reduce overall costs.

1. Introduction

Nearly 60% of the calculated U.S. offshore wind energy resource potential is over waters more than 60 m deep, where development of fixed-bottom offshore wind turbines is both technically and economically prohibitive (Musial et al., 2016a). Though this area is estimated to be able to provide the equivalent of the entire U.S. annual electricity consumption if tapped with power plants composed of floating offshore wind turbines (FOWTs) (Musial et al., 2016b), the high cost of state-of-the-art FOWTs poses a formidable barrier to its exploitation.

In response to this problem, the U.S. Department of Energy (DOE)'s Advanced Research Projects Agency-Energy (ARPA-E) kicked-off a new program: Aerodynamic Turbines Lighter and Afloat with Nautical Technologies and Integrated Servo-control (ATLANTIS). This program, among other goals, seeks to promote the design of radically new FOWTs by maximizing their rotor-area-to-total-weight ratio while either maintaining or ideally increasing turbine generation efficiency. This would yield levelized cost of energy (LCOE) values that make deep water sites economically viable to FOWT wind development. The program encourages the application of control co-design (CCD) methodologies to integrate feedback control and dynamic interaction principles as the primary drivers of the design.

The Floating Wind Technology Company together with the department of Electrical Engineering at Colorado School of Mines (CSM) and a multidisciplinary team comprised of the National Renewable Energy Laboratory (NREL), the University of Colorado at Boulder (CU), the University of Virginia (UVA), and the American Bureau of Shipping (ABS) are involved in a project named Ultra-flexible Smart Floating Offshore Wind Turbine (USFLOWT). USFLOWT is funded by ARPA-E's ATLANTIS program and has the goal of reducing FOWT's LCOE via the innovative platform SpiderFLOAT (SF) supporting a state-of-the-art, 10-MW class wind turbine.

*Corresponding author
✉ r.damiani@floatingwindtech.com (R. Damiani)
🌐 www.floatingwindtech.com (R. Damiani)
ORCID(s): 0000-0002-8199-1373 (R. Damiani)

The SF substructure (Fig. 1) was conceived to enable CCD optimization including smart control systems for mass minimization, system stability, and performance. The components of the substructure are fully modular and designed for ease of manufacturing (through a combination of local-content prefab and onsite manufacturing), transport, and installation. The low fixity level of the joints transfers minimum bending loads among the members, thus reducing demand on structural resistance, and allowing for tunable system hydrodynamic stiffness. Rather than responding to the waves as a rigid unit, SF's compliant members can have individual dynamics, thus can mitigate wave hydrodynamic forces and damp unwanted energy with only a reduced portion transferred to the rotor-nacelle-assembly and tower. Compared to currently deployed heavy and stiff floaters of oil and gas (O&G) derivation (e.g., Fig. 2), SF's innovative ultracompliant approach becomes evident. However, this ultra-flexible layout gives rise to complex dynamics and therefore requires a robust control system to maintain stability and performance.
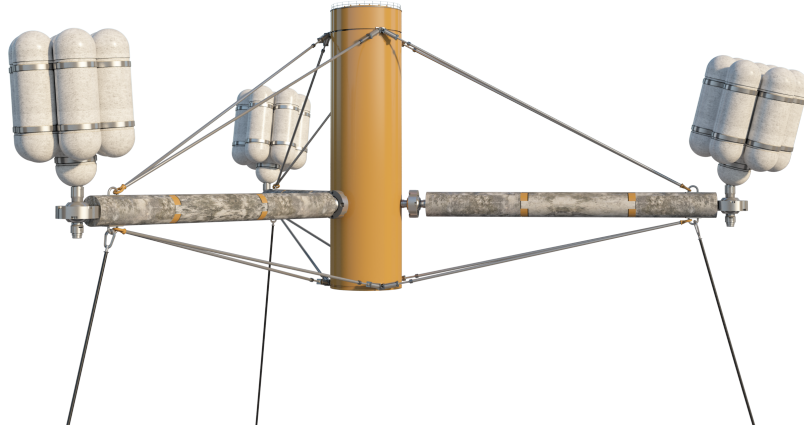

Figure 1: Artist rendering of the SF substructure (source: J. Bauer, NREL).
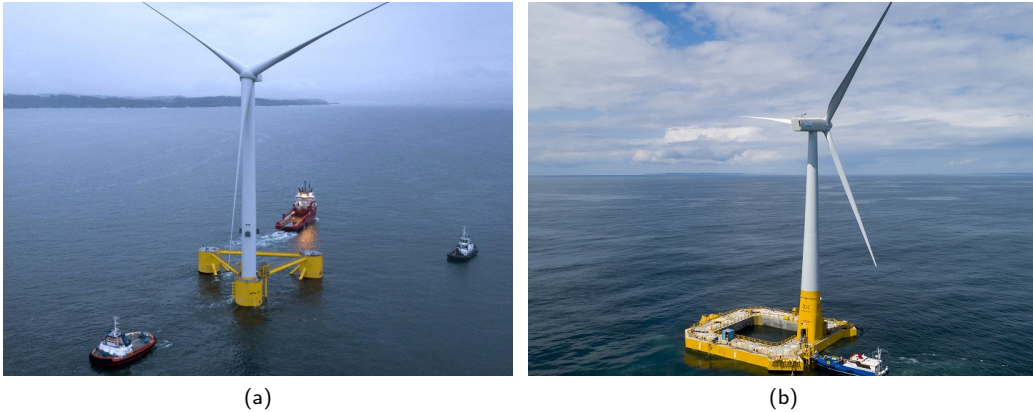

(a)   (b)

Figure 2: Typical FOWTs currently in operation; (a) PPI's WindFLOAT (source Principal Power, Inc.); (b) Ideol's FloatGen (source Ideol).

SF makes use of reinforced concrete (RC) with an effective pre-stressing strategy realized via the very same stay-cables that guarantee the structural shape and functional integrity of the floater. RC structures can offer ample versatility in design and construction, can take advantage of local material and labor resources, are virtually maintenance free, feature cost-competitive material (concrete and steel) utilization, and have excellent fatigue and dynamic damping properties. The SF can largely be manufactured at port and with relatively small footprint. The legs are modular, with three or more segments, precast or slipformed at port. The leg segments can be stacked in a relatively small staging area, and picked up and moved to the assembly dock where they are bolted and grouted at their connections and installed

onto the SF. The central stem is also fabricated out of RC, assembled in bolted/grouted segments, and benefits from the pre-compression realized by the same stay (post-tensioning) cables. This modular, industrialized construction method allows for simultaneous multi-component fabrication and parallel staging with minimum real-estate usage, therefore mitigating the drawbacks often attributed to concrete construction. The buoyancy cans are comprised of bundles of glass-fiber reinforced plastic (GFRP) pressure vessels tied together and linked to the ends of the legs during assembly. The cans can also be fabricated on-site via filament winding.

In this study, we developed an engineering model to determine the internal loads on the cables and legs that can then be used to size both components. Whereas this model can help size the SF central stem, the stem design will be the object of a future article. In our approach, the classical linear elastic beam theory was analytically extended to include second-order effects (e.g., P-δ moment amplification) that could lead to both an amplification of the bending stresses and to global instability. The theory was used to help close a system of equations for the static balance of the leg-cable subsystem that would otherwise be indeterminate.

The new theory was developed from first principles and implemented into a Python code, i.e., SpiderFLOAT Offshore Floater Tool for Sizing (SOFT4S), that can leverage OpenMDAO's optimization framework (Gray et al., 2019) and the aero-hydro-servo-elastic (AHSE) tools OrcaFLEX (Orcina Ltd, 2020) and OpenFAST (Jonkman, 2013). SOFT4S can in fact produce input files for these AHSE codes after determining the preliminary dimensions of the SF. In turn, AHSE simulations provide more accurate estimates of the external loads needed to run SOFT4S. As such, SOFT4S allows for quick turn-around analyses of the USFLOWT support structure and system dynamics within the CCD iterations. Numerically efficient tools, such as the one we propose, are, in fact, needed to guide the floater preliminary design through a multidisciplinary optimization infrastructure thereby rendering an effective balance between system mass (thus costs) and performance. Additionally, within OpenMDAO's framework, when coupled to a system and plant cost model (e.g., Dykes et al., 2011), SOFT4S allows for the full gamut of component investigations to arrive at LCOE-optimized wind turbine and/or power plant layout.

In stand-alone mode, SOFT4S aids the designer in the search for an optimal preliminary configuration (e.g., stem, leg, stay cable geometry) for given environmental loading conditions. The optimization criteria (e.g., minimum sub-component mass or overall total structural mass) are customizable depending on the user's needs. SOFT4S also allows for parametric investigations and sensitivity analyses of both external factors and geometric variables that may drive the characteristics of the structure, thereby illustrating their impact on the mass, stiffness, strength, reliability, and expected costs.

SOFT4S can determine, among other design variables, the required leg length, its outer and inner diameters, its embedded reinforcement, and the number, size, and prestress values of the cables. A set of functions implement structural code checks per ACI (2014) to verify the leg cross-section under serviceability limit state (SLS) and ultimate limit state (ULS) and at various stations along the span. The design (fixed) parameters (inputs to the tool) include: lumped and distributed hydrodynamic loads, joint overall geometry, buoyancy and weight of the cans, and material characteristics. The hydrodynamic distributed loads are derived from AHSE simulations. Acceptable ranges for the design variables (e.g., maximum and minimum diameters, prestress levels, rebar and hoop reinforcement size and numbers) must also be provided as input parameters.

The model has undergone preliminary verification. A future version of the model will include a refined fatigue treatment, and automatic selection of standard dimensions for the various subcomponents.

This document discusses the geometry of the SF in Section 2, with an overview of the nomenclature used throughout this study. The load determination problem and its indeterminate nature are presented in Section 3. Section 4 first presents the newly developed analytical beam theory and then a compatibility approach to make the force system of equations determinate. Section 5 discusses the necessary steps for SLS and ULS leg verification. In Section 6, SOFT4S is used to derive a preliminary design for legs and cables of the SF, and a cross-verification of the newly developed model is performed against a commercial finite-element method (FEM) package. A summary of SOFT4S's development and planned future research are provided in Section 7.

2. Geometry and Coordinate Systems

The geometry of the SF main components is shown in Fig. 3. Also shown are the symbols used in this study to denote the main design variables. Due to the 120 deg symmetry, for simplicity we will focus on ⅓ of the SF and analyze one leg with its cable systems. Although the analytical development is carried out in the vertical plane for increased clarity, the lateral plane statics is analogous and the axis-symmetric nature of the leg allow for a combination

of the loads in a new coordinate system.

The typical mooring line (not shown) is connected via a fairlead at the joint between the leg and the buoyancy can.

There are two main coordinates systems employed in this development: one is the 'global' reference frame also shown in Fig. 3, and the other is the beam 'local' coordinate system shown in Fig. 4. The global reference frame has
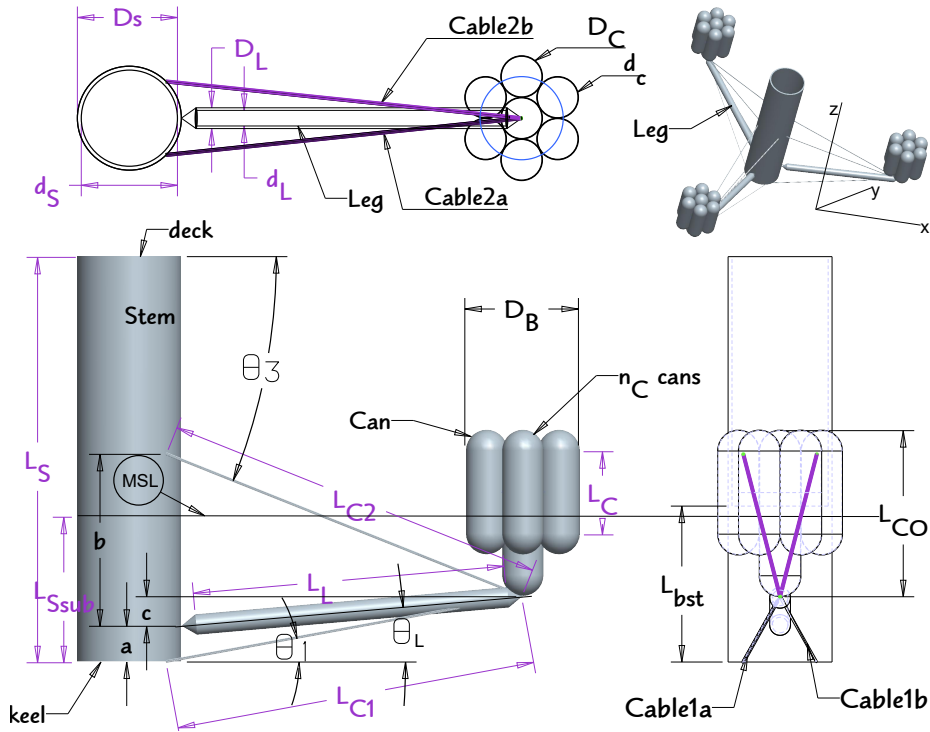
Figure 3: From top-left corner counterclockwise: top, front, side, and isometric views of the SF's single leg-cable sub-assembly with nomenclature used throughout this paper.
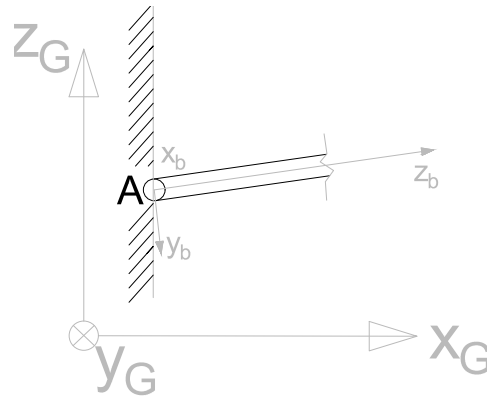
Figure 4: SF global reference frame and leg local reference frame used throughout this development.

the origin at the intersection of the mean sea level plane and the central stem axis in the undisturbed configuration, X_G is along the nominal wind direction, Z_G is vertical and pointing upward, and Y_G per right-hand rule. In this study, the rigid body rotation (pitch, roll, and yaw expected less than ~10°) are assumed negligible without losing in generality. AHSE simulations proved that the largest distributed hydrodynamic loads exerted on the leg (inertial plus viscous drag components on the order of 1×10^3 N m^{-1}) are about an order of magnitude less than the buoyancy component (on the order of 1×10^4 N m^{-1}).

The leg local reference frame (Fig. 4) has origin in A, joint between leg and central stem, z_b is along the leg axis, x_b is perpendicular to z_b and nominally in the horizontal plane, and y_b points downward following the right-hand rule.

3. The Load Determination Problem

The SF in Fig. 3 can be reduced to an assembly of beams and tension-only members (the cables). In Fig. 5, we examine the forces acting on the hinge B. Here we consider the action of the twin cables ($C1_a$,$C1_b$ and $C2_a$,$C2_b$
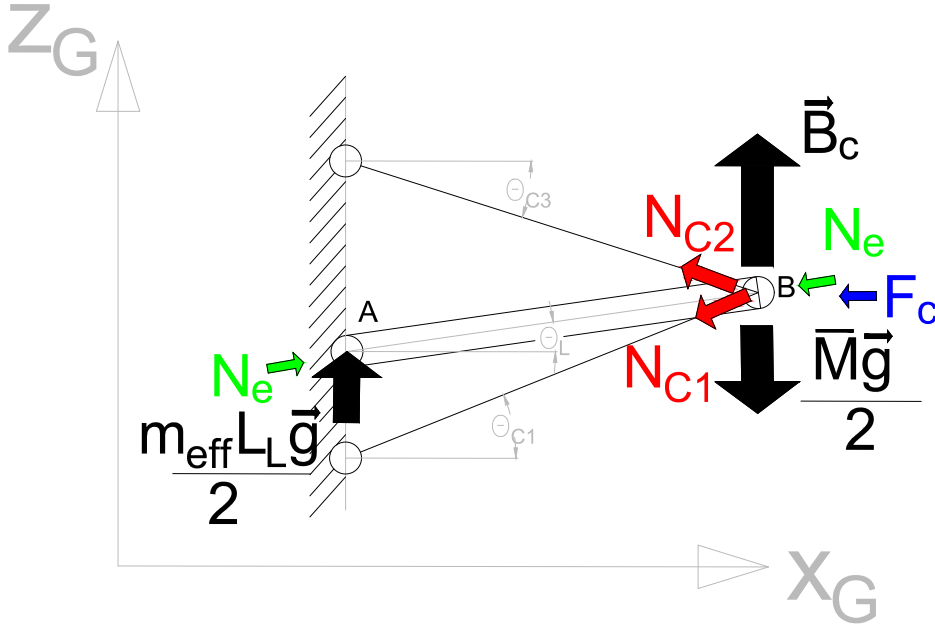

Figure 5: Diagram showing the force balance at joint B in the vertical plane containing the central stem axis and the leg. Meaning of symbols in main text and Section 3.1.

) in the vertical plane $X_G Z_G$. As a simplification in the treatment of this structure, an equivalent single cable with a doubled cross-sectional surface area replaces each cable pair; these equivalent cables are denoted by $C1$ and $C2$, for the lower and upper cable, respectively. Because of the expected SF geometry, the difference between the tension calculated for the equivalent cable and the sum of the associated cable pair tensions is less than 0.6%. Accordingly, we will denote the resultants of the cable tensions in the vertical plane as N_{C1} and N_{C2}, for the lower and upper cable pairs, respectively.

The lateral plane statics can be treated in a similar fashion to what will be presented here; for sake of clarity and because the driving loads resulted to be those associated with the vertical plane statics, we concentrate on the latter plane and forgo the treatment of the former in this article. The lateral component of the cable tension as well as the leg shear and bending in the lateral plane, however, are fully included in our software SOFT4S implementation.

Finally, the structure in Fig. 5 is shown with the stem in the upright position. As mentioned above, a non-nil heel angle has to be expected during turbine operation ($\lesssim 10°$), but the theory development is virtually unchanged when accounting for a constant bias in the platform attitude angles. For sake of clarity, in this paper, we omit the small listing angle effects, though SOFT4S's implementation includes these details as well.

3.1. Statically Indeterminate Structural System

We can write the balance of forces at B, in the global coordinate system (X_G, Z_G), as in Eq. (1):

$$\begin{cases} N_{C1} \cos\left(\theta_{C1}\right) - N_e \cos\left(\theta_L\right) + N_{C2} \cos\left(\theta_{C2}\right) + F_c = 0 \\ -N_{C1} \sin\left(\theta_{C1}\right) + N_e \sin\left(\theta_L\right) + N_{C2} \sin\left(\theta_{C2}\right) + B_{eff} = 0 \end{cases} \tag{1}$$

where N_e is the equivalent force aligned with $\overline{AB}$ and acting onto the leg, therefore $-N_e$ is the reaction from the leg onto joint B; θ_{C1}, θ_L, θ_{C2} are the angles between the normal to the stem axis and the various members, after any deflection occurred; F_c is the horizontal component of the force exerted by the can and mooring line onto the leg, due to hydrodynamic and inertial loading, and assumed known; B_{eff} is the effective buoyancy magnitude at joint B, accounting for other hydrodynamic forces, for the weight of the buoyancy can bundle, half the weight of the cables, and half the weight of the leg as shown in Eq. (2):

$$B_{eff} = |\mathbf{B_c}| - \frac{(m_{eff}L_{L0} + 2M_C + M_{C1} + M_{C2}) * g}{2} = |\mathbf{B_c}| - \frac{\bar{M}g}{2} \tag{2}$$

where $\mathbf{B_c}$ is the buoyancy force at B; m_{eff} is the effective mass per unit length, to account for hydrostatic buoyancy, hydrodynamic, and distributed inertial loads; L_{L0} is the leg length in the undeformed condition; M_C is the mass of the buoyancy can bundle at B; M_{C1} is the mass of cable set $C1$; M_{C2} is the mass of cable set $C2$; and g is the magnitude of the gravitational acceleration.

Assuming the angles θ_{C1}, θ_L, and θ_{C2} as shown in Fig. 5 are known, the unknowns are then three: N_{C1}, N_{C2}, N_e. Note that because all of the forces intersect at B, the resultant moment is intrinsically nil, and therefore the system of equations is underdetermined. It is straightforward to prove that the beam system is, in fact, one time hyperstatic. This means that to close the system of equations in Eq. (1), one must account for the stiffness of the members, and therefore obtain a new equation.

By examining the displacement of the joint B, from B_0, i.e., its position before any load application, to its final position, one could write an equation linking the displacement (u_B, w_B) in the global reference frame to that in the local beam reference frame, as shown in Eq. (3) and Fig. 6:

$$w(L_{L0}) = u_B \cos \theta_L + w_B \sin \theta_L \tag{3}$$

So one could write the expression for $w(L_{L0})$ from the elastic line theory applied to the leg member as a function of
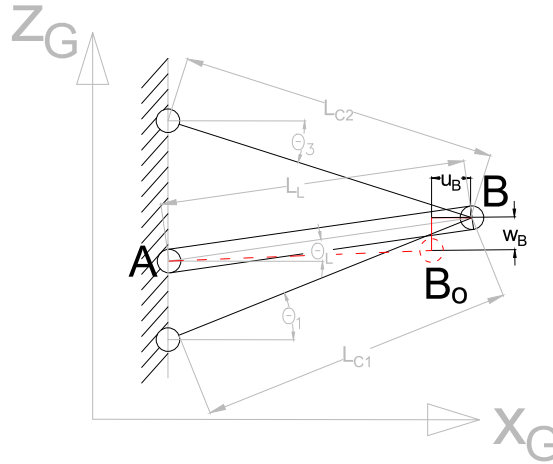
Figure 6: Two-dimensional displacement of the B joint (u_B, w_B) under externals forces. $L_{C1,f}$, $L_{C2,f}$, and L_L denote the lengths, in the deflected configuration, of cables $C1$ and $C2$, and leg, respectively. The meaning of other symbols is given in the main text.

the stiffness properties of the leg and then use Eq. (3) to tie that to the overall system geometry and close the system in Eq. (1).

In the next Section, an innovative analytical beam theory is provided to help solve the indeterminate structural system.

4. Elastic Beam Theory Extension and Solution of the Indeterminate Structure

A new theory is developed that is nonlinear in terms of final configuration geometry, but still linear in terms of material stress-strain relationship. In this Section, we highlight the main equations of this new analytical method, but

the full mathematical development is offered in Appendix D. In Sections 4.1–4.3, the classical beam theory is modified to include a contribution from the bending deformation to the normal force, by retaining a second order term in the Taylor expansion of the axial strain. This allows to write the equilibrium of the external loads and internal forces on the deformed configuration of the structure. In turn, this allows to include changes in the geometric stiffness of the leg, and therefore second-order ('P-δ') effects associated with potential buckling and instability. Most traditional methods for incorporating these effects in the analysis of structures are based on time-consuming iterative techniques (Wilson, 2002; Powell, 2010). In Section 4.4, the indeterminate system of equations presented in the previous Section is augmented with a compatibility equation derived from the modified beam theory, which allows its solution.

4.1. Derivation of the Beam Internal Loads and Transverse Deflection

Given the slender geometry of the typical SF leg, it is reasonable to treat the leg as an ideal Euler-Bernoulli beam (Timoshenko and Young, 1965). We start this development by analyzing an infinitesimal segment of a leg as shown in Fig. 7. In Eq. (4), the balance of the forces acting on the infinitesimal beam segment is written along y_b and z_b in
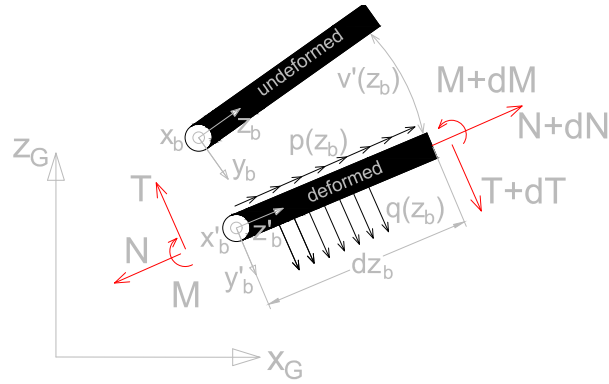

Figure 7: Infinitesimal segment of beam in its deformed condition and external and internal loads acting on it. Meaning of symbols in main text.

the local (undeformed) coordinate system:

$$\begin{cases} d\left(N\cos\left(v'\right)\right) - d\left(T\sin\left(v'\right)\right) + p(z_b)dz_b = 0 \\ d\left(T\cos\left(v'\right)\right) + d\left(N\sin\left(v'\right)\right) + q(z_b)dz_b = 0 \end{cases} \tag{4}$$

where N is the axial load at the span station of interest; v is the deflection normal to beam axis in the y_b direction; T is the shear component along the y-axis at span station of interest; $p(z_b)$ is the component of the external, distributed static loading along the beam z_b axis; $q(z_b)$ is the component of the external, distributed static loading along the beam y_b axis; d denotes the differential operator. Throughout this paper, the prime symbols $'$, $''$, and $'''$ denote first, second, and third order spatial derivatives relative to z_b, respectively.

Assuming a constant cross-section leg, $p(z_b)$ and $q(z_b)$ can be written as in Eq. (5):

$$\begin{cases} p(z_b) = -m_{eff}g\sin\left(\theta_L\right) \\ q(z_b) = m_{eff}g\cos\left(\theta_L\right) \end{cases} \tag{5}$$

where θ_L is the angle between global x and leg; and $m_{eff}(z_b) = m_{eff}$ is the effective mass per unit length, to account for hydrostatic buoyancy, hydrodynamic, and distributed inertial loads. Results obtained from AHSE simulations demonstrated that considering $m_{eff}g$ as uniform along the leg span is a valid approximation. The distributed buoyancy is, in fact, the largest contribution from the hydrodynamic actions and the peak values of other loading components do not vary significantly along the span. Under these hypotheses, and considering the boundary conditions at z_b=0 m (see also Fig. 17), Eq. (4) can be integrated to give expressions for N and T as shown in Eq. (6):

$$\begin{cases} N = -\left[N_e + m_{eff}g\sin\left(\theta_L\right)\left(\dfrac{L_{L0}}{2} - z_b\right)\right]\cos\left(v'\right) + m_{eff}g\cos\left(\theta_L\right)\left(\dfrac{L_{L0}}{2} - z_b\right)\sin\left(v'\right) \\ T = \left[N_e + m_{eff}g\sin\left(\theta_L\right)\left(\dfrac{L_{L0}}{2} - z_b\right)\right]\sin\left(v'\right) + m_{eff}g\cos\left(\theta_L\right)\left(\dfrac{L_{L0}}{2} - z_b\right)\cos\left(v'\right) \end{cases} \tag{6}$$

Note that the reaction at the joint A was divided into two contributions: one aligned with the global Z_G and one (N_e) aligned as $\overline{AB}$. It is straightforward to verify that the vertical component must be equal to 1/2 the effective weight of the beam. No other force can act on joint A for equilibrium of the leg.

The balance of moments about the right end of the beam segment and along the local $x_b \equiv Y_G$ can be written as in Eq. (7):

$$M' - \left[N \sin\left(v'\right) + T \cos\left(v'\right)\right]\left(1 + w'\right) + \left[N \cos\left(v'\right) - T \sin\left(v'\right)\right]v' = 0 \tag{7}$$

where M is the bending moment about the local x_b axis at the span station of interest.

Making use of Eq. (6), Eq. (7) can rewrite as in Eq. (8):

$$M' = \left[m_{eff}g\cos\left(\theta_L\right)\left(\frac{L_{L0}}{2} - z_b\right)\right]\left(1 + w'\right) + \left[N_e + m_{eff}g\sin\left(\theta_L\right)\left(\frac{L_{L0}}{2} - z_b\right)\right]v' \tag{8}$$

By integrating Eq. (8) between $z_b = 0\,\mathrm{m}$ and the generic $\hat{z}_b$, and making use of the boundary conditions at the hinge at $z_b = 0\,\mathrm{m}$, one arrives at the expression for the bending moment about x_b (Eq. (52)). By neglecting further shear contributions to the curvature of the beam axis, denoting by E_c the concrete Young's modulus, and by J_{xxceff}[1] the normalized concrete cross-sectional second area moment of inertia, the Euler approximation $M = -E_c J_{xxceff} v''$ could be used. This would result into a second order, linear ordinary differential equation (ODE) for the deflection v. This ODE, however, does not lend itself to an analytical solution, hence two simplifications are performed on Eq. (8).

The first simplification neglects the terms containing w. In concrete, it is common to assume a maximum compressive strain at ULS $\epsilon_{cu} \simeq -0.003$, thus the term $(1 + w')$ in Eq. (8) can be taken as 1. However, even with this simplification, the resulting ODE has variable coefficients and does not have a readily useful analytical solution.

Therefore, a second simplification consists of replacing the term $m_{eff}g\sin\left(\theta_L\right)\left(\frac{L_{L0}}{2} - z_b\right)$ that multiplies v' with its mean value in $(0, L_{L0})$, which can be easily proven to be 0. Eq. (8) can now be analytically integrated with nil boundary conditions at A to return an expression for v as in Eq. (9):

$$v(z_b) = \frac{m_{eff}g}{N_e\alpha^2}\cos(\theta_L)\left[\cos(\alpha z_b) + \frac{1 - \cos(\alpha L_{L0})}{\sin(\alpha L_{L0})}\sin(\alpha z_b) - \frac{L_{L0} - z_b}{2}z_b\alpha^2 - 1\right] \tag{9}$$

where α is taken as:

$$\alpha = \sqrt{\frac{N_e}{E_c J_{xxceff}}} \tag{10}$$

Note that for $\alpha L_{L0} \to 0$ the expression in Eq. (9) goes to infinity, i.e., we have the Eulerian buckling condition (Timoshenko and Gere, 1963) of $\alpha L_{L0} = i_c\pi$ $(i_c = 1, 2..\infty)$ which would render the critical load ($N_{e,cr}$):

$$N_{e,cr} = \frac{\pi^2 E_c J_{xxceff}}{L_{L0}{}^2}i_c{}^2 \tag{11}$$

4.2. Nonlinear Constitutive Equation and Derivation of the Beam Axial Deflection

To complete this extension of the beam theory, we seek to find an expression for $w(z_b)$ that can be used to solve Eq. (3).

By retaining up to second-order terms in the Taylor expansion of its definition, the total strain ϵ can be expressed as the sum of the axial strain, w', and the shortening of the beam due to bending, $\frac{1}{2}v'^2$ (see Appendix D.1 and Fig. 7). The axial force N can therefore be expressed as in Eq. (12) introducing a nonlinearity in the beam constitutive equation:

$$N = E_c A_{Leff}\epsilon = E_c A_{Leff}\left[\frac{1}{2}v'^2 + w'\right] \tag{12}$$

where A_{Leff}[1] is the concrete, leg cross-sectional area normalized for nonprestressed rebar (see also Section 5). Starting from Eq. (6), and acknowledging the constitutive equation in Eq. (12), one can write a partial differential equation

---

[1]See Section 5 for its definition.

(PDE) for w that includes terms in v. Accounting for small angle deflection approximation ($v' << 1$, thus $\cos(v') \simeq 1$ and $\sin(v') \simeq v'$), and replacing $v(z_b)$ for the expression in Eq. (9), and by integrating, w can be attained as in Eq. (13):

$$
\begin{aligned}
w(z_b) = &-\frac{1}{E_c A_{Leff}} \left[N_e * z_b + m_{eff} g \sin\left(\theta_L\right) \left(\frac{L_{L0} z_b - z_b^2}{2} \right) \right] \\
&+ \frac{\left(m_{eff} g \cos(\theta_L) \right)^2}{E_c A_{Leff} N_e} \left[\frac{1}{\alpha^2} \left(\frac{L_{L0}}{2} - z_b \right) \cos\left(\alpha z_b\right) - \frac{L_{L0}}{2\alpha^2} + \frac{\sin\left(\alpha z_b\right)}{\alpha^3} \right. \\
&+ \frac{6 L_{L0} z_b^2 - 3 L_{L0}^2 z_b - 4 z_b^3}{12} + \tan\frac{\alpha L_{L0}}{2} \left(\frac{\sin(\alpha z_b)}{\alpha^2} \left(\frac{L_{L0}}{2} - z_b \right) + \frac{1}{\alpha^3} \left(1 - \cos\left(\alpha z_b\right) \right) \right) \Big] \\
&+ \frac{\left(m_{eff} g \cos(\theta_L) \right)^2}{2 N_e^2 \alpha^3} \left[-\frac{\alpha z_b}{2} + \frac{\sin\left(2\alpha z_b\right)}{4} + \frac{-4 z_b^3 + 6 L_{L0} z_b^2 - 3 L_{L0}^2 z_b}{12}\alpha^3 \right. \\
&- \tan^2\frac{\alpha L_{L0}}{2} \left(\frac{\alpha z_b}{2} + \frac{\sin\left(2\alpha z_b\right)}{4} \right) + 2\sin\left(\alpha z_b\right) - \alpha L_{L0} + \alpha\left(L_{L0} - 2 z_b\right)\cos\left(\alpha z_b\right) \\
&+ \tan\frac{\alpha L_{L0}}{2} \left(1 - \cos^2\left(\alpha z_b\right) \right) + \tan\frac{\alpha L_{L0}}{2} \left(2 - 2\cos\left(\alpha z_b\right) + \alpha(L_{L0} - 2 z_b)\sin(\alpha z_b) \right) \Big]
\end{aligned}
\tag{13}
$$

4.3. Summary of the Extended Elastic Beam Theory

Including the approximations assumed so far, the beam internal loads can be written as in Eq. (14):

$$
\begin{cases}
N = -\left[N_e + m_{eff} g \sin\left(\theta_L\right) \left(\frac{L_{L0}}{2} - z_b \right) \right] + m_{eff} g \cos\left(\theta_L\right) \left(\frac{L_{L0}}{2} - z_b \right) v' \\
T = \left[N_e + m_{eff} g \sin\left(\theta_L\right) \left(\frac{L_{L0}}{2} - z_b \right) \right] v' + m_{eff} g \cos\left(\theta_L\right) \left(\frac{L_{L0}}{2} - z_b \right) \\
M = -E_c J_{xxceff} v''
\end{cases}
\tag{14}
$$

where v, v', v'' are given in Eq. (15)

$$
\begin{cases}
v(z_b) = \frac{m_{eff} g}{N_e \alpha^2} \cos(\theta_L) \left[\cos(\alpha z_b) + \frac{1 - \cos(\alpha L_{L0})}{\sin(\alpha L_{L0})} \sin(\alpha z_b) - \frac{L_{L0} - z_b}{2} z_b \alpha^2 - 1 \right] \\
v'(z_b) = \frac{m_{eff} g}{N_e \alpha} \cos(\theta_L) \left[\cos(\alpha z_b) * \frac{1 - \cos(\alpha L_{L0})}{\sin(\alpha L_{L0})} - \sin(\alpha z_b) - \left(\frac{L_{L0}}{2} - z_b \right) \alpha \right] \\
v''(z_b) = \frac{m_{eff} g}{N_e} \cos(\theta_L) \left[-\sin(\alpha z_b) * \frac{1 - \cos(\alpha L_{L0})}{\sin(\alpha L_{L0})} - \cos(\alpha z_b) + 1 \right]
\end{cases}
\tag{15}
$$

and where α is given in Eq. (10) and the displacement w can be written as in Eq. (13).

4.4. Compatibility Equation and Solution of the Structural System

From Eq. (3) and Eq. (13), the compatibility equation needed to close the dertermined system balance is obtained by calculating $w(L_{L0})$:

$$w(L_{L0}) = u_B \cos \theta_L + w_B \sin \theta_L =$$

$$= -\frac{N_e * L_{L0}}{E_c A_{Leff}} + \frac{\left(m_{eff} g \cos(\theta_L)\right)^2}{E_c A_{Leff} N_e} \left[-\frac{L_{L0}}{2\alpha^2} \cos\left(\alpha L_{L0}\right) - \frac{L_{L0}}{2\alpha^2} + \frac{\sin\left(\alpha L_{L0}\right)}{\alpha^3} - \frac{L_{L0}^3}{12} \right.$$

$$+ \tan\frac{\alpha L_{L0}}{2} \left(-\frac{\sin(\alpha L_{L0})}{\alpha^2}\frac{L_{L0}}{2} + \frac{1}{\alpha^3}\left(1 - \cos\left(\alpha L_{L0}\right)\right) \right) \Big]$$

$$+ \frac{\left(m_{eff} g \cos(\theta_L)\right)^2}{2N_e^2\alpha^3} \left[-\frac{\alpha L_{L0}}{2} + \frac{\sin\left(2\alpha L_{L0}\right)}{4} - \frac{L_{L0}^3}{12}\alpha^3 - \tan^2\frac{\alpha L_{L0}}{2}\left(\frac{\alpha L_{L0}}{2} + \frac{\sin\left(2\alpha L_{L0}\right)}{4} \right) \right.$$

$$+ 2\sin\left(\alpha L_{L0}\right) - \alpha L_{L0} - \alpha L_{L0} \cos\left(\alpha L_{L0}\right) + \tan\frac{\alpha L_{L0}}{2}\left(1 - \cos^2\left(\alpha L_{L0}\right)\right)$$

$$+ \tan\frac{\alpha L_{L0}}{2}\left(2 - 2\cos\left(\alpha L_{L0}\right) - \alpha L_{L0}\sin(\alpha L_{L0})\right) \Big] \tag{16}$$

Performing some algebraic and trigonometric reductions, and recognizing that $w(L_{L0}) = L_L - L_{L0}$ (where L_L is the leg length in the deformed condition), Eq. (16) is rewritten together with the remainder of the structural system load balance equations as in Eq. (17):

$$\begin{cases} N_{C1}\cos\left(\theta_{C1}\right) - N_e\cos\left(\theta_L\right) + N_{C2}\cos\left(\theta_{C2}\right) + F_c = 0 \\[4pt] -N_{C1}\sin\left(\theta_{C1}\right) + N_e\sin\left(\theta_L\right) + N_{C2}\sin\left(\theta_{C2}\right) + B_{eff} = 0 \\[4pt] \dfrac{E_c A_{Leff}(L_L - L_{L0})}{L_{L0}} - \left[-N_e - \dfrac{\left(m_{eff} g\cos(\theta_L)\right)^2}{12 E_c J_{xxceff}} L_{L0}^4 \left[\dfrac{1}{L_{L0}^2\alpha^2} + \dfrac{12}{L_{L0}^4\alpha^4} - \dfrac{24}{L_{L0}^5\alpha^5}\tan\dfrac{\alpha L_{L0}}{2} \right] \right. \\[12pt] \left. -E_c A_{Leff}\dfrac{\left(m_{eff} g\cos(\theta_L)\right)^2}{24 E_c^2 J_{xxceff}^2} L_{L0}^6 \left[\dfrac{1}{\alpha^4 L_{L0}^4} - \dfrac{60}{L_{L0}^7\alpha^7}\tan\dfrac{\alpha L_{L0}}{2} + \dfrac{24}{\alpha^6 L_{L0}^6} + \dfrac{12\left(1 - \cos(\alpha L_{L0})\right)}{\alpha^6 L_{L0}^6\sin^2\left(\alpha L_{L0}\right)} \right] \right] = 0 \end{cases} \tag{17}$$

Note that L_L is a function of θ_L, i.e., the final angle assumed by the line connecting $\overline{AB}$. The unknowns in Eq. (17) are N_e, u_B, and w_B; all the other variables, in fact, (namely, N_{C1}, N_{C2}, L_L, θ_{C1}, θ_{C2}, θ_L, and the final cable lengths, i.e., $L_{C1,f}$ $L_{C2,f}$) can be expressed as a function of these three unknowns as it is shown below.

The SF assembly sequence starts with the central stem resting on a stand, while the legs are being positioned at the correct elevation. The cables are then connected at the As and Bs hinges, and pre-tensioning of the $C1$ and $C2$ cable sets occurs to reach a preset tensioning value (e.g., σ_{C1pt}, σ_{C2pt}) as recorded by the tensioners. Once in the water, with the system fully assembled, the hinge at B would assume a new deflected position i.e., (u_B, w_B) that also directly affects the loads in the cables.

First, the cable tensions, N_{C1} and N_{C2}, can be thought as given by the superposition of the loads reached during the prestressing phase (with prescribed stress values of σ_{C1pt} and σ_{C2pt}, respectively) and those due to the assumed deflection of the B hinge (i.e., (u_B, w_B)) when in the water during operation. The cable tensions can therefore be written as in Eq. (18):

$$N_{C1} = N_{C1}(u_B, w_B, A_{C1}, \sigma_{C1pt}) = E_p * A_{C1} * \epsilon_{C1} = E_p * A_{C1} * \left[\frac{L_{C1,f} - L_{C1,0}}{L_{C1,0}} + \frac{\sigma_{C1pt}}{E_p} \right]$$

$$N_{C2} = N_{C2}(u_B, w_B, A_{C2}, \sigma_{C2pt}) = E_p * A_{C2} * \epsilon_{C2} = E_p * A_{C2} * \left[\frac{L_{C2,f} - L_{C2,0}}{L_{C2,0}} + \frac{\sigma_{C2pt}}{E_p} \right] \tag{18}$$

By considering the geometry shown in Fig. 6, and via vector additions, we can then derive expressions for $L_{C1,f}$, $L_{C2,f}$, L_L, θ_{C1}, θ_{C2}, θ_L (Eq. (19)) as functions of their initial (pre-deflected) values ($L_{C1,0}$, $L_{C2,0}$, L_{L0}, $\theta_{C1,0}$, $\theta_{C2,0}$,

$\theta_{L,0}$) and the deflection (u_B, w_B):

$$
\begin{aligned}
L_{C1,f} &= \sqrt{L_{C1,0}{}^2 + 2\left(u_B \cos\theta_{C1,0} + w_B \sin\theta_{C1,0}\right) L_{C1,0} + u_B{}^2 + w_B{}^2} \\
L_{C2,f} &= \sqrt{L_{C2,0}{}^2 + 2\left(u_B \cos\theta_{C2,0} - w_B \sin\theta_{C2,0}\right) L_{C2,0} + u_B{}^2 + w_B{}^2} \\
L_L &= \sqrt{L_{L0}{}^2 + 2\left(u_B \cos\theta_{L,0} + w_B \sin\theta_{L,0}\right) L_{L0} + u_B{}^2 + w_B{}^2} \\
\theta_{C1} &= \sin^{-1}\frac{L_{C1,0} \sin\theta_{C1,0} + w_B}{L_{C1,f}} \\
\theta_{C2} &= \sin^{-1}\frac{L_{C2,0} \sin\theta_{C2,0} - w_B}{L_{C2,f}} \\
\theta_L &= \sin^{-1}\frac{L_{L0} \sin\theta_{L,0} + w_B}{L_L}
\end{aligned}
\tag{19}
$$

The system of equations in Eq. (17) can thus be solved for the unknowns N_e, u_B, w_B with the following fixed parameters:

- Geometry: $L_{C1,0}$, $L_{C2,0}$, L_{L0}, $\theta_{C1,0}$, $\theta_{C2,0}$, $\theta_{L,0}$

- Structural Properties: E_c, E_p, A_{Leff}, A_{C1}, A_{C2}, σ_{C1pt}, σ_{C2pt}, J_{xxceff}

- Masses and Loads: m_{eff}, M_C, M_{C1}, M_{C2}, B_{eff}, F_c

Note that to account for the effective loads on the leg and $C1$ cables, the m_{eff}, M_{C1}, and B_{eff} terms are appropriately modified to include distributed buoyancy effects, hydrodynamic viscous and inertial drag, and structural inertia loading.

5. Leg Dimensioning

The design verification against SLS and ULS of one of SF's RC legs is performed following the steps highlighted in this Section. Here, we focus solely on the structural design aspects, and assume that the leg hydrodynamic requirements have already been addressed, whereby specifying, for example, minimum leg length, maximum leg mass and/or buoyancy. The latter demands would be verified by the external optimization loop of SOFT4S.

Generally speaking, the structural verification consists of satisfying SLS, fatigue limit state (FLS), accidental limit states (ALS), and ULS design requirements. In the case of SF, boat impacts must be considered as concentrated loads at critical locations along the span of a leg and central stem. Other potential accidental load cases would require investigating the loss of a stay cable. These aspects are certainly important and will require dedicated studies to assess the level of acceptable risk and redundancy required. In this paper, we concentrate on SLS and ULS, which should also guarantee a certain level of safety against ALS and FLS at least for the concrete leg. A considerable amount of research is still ongoing on reinforced concrete fatigue, but general rules based on damage equivalent load (DEL) and damage equivalent stress (DES) (FIB, 2013; ECS, 2004; DNV-GL, 2018) can be employed with the internal load determination model as described in this paper. Furthermore, simplified methods (ECS, 2004) check for an adequate fatigue life by using the maximum and minimum compressive stress under the most typical load combination. Therefore, the methods described in this paper can be directly applied to assess the fatigue life of cables and leg. We will address these aspects in a future article.

An additional verification should be performed on the system and component eigenfrequencies to ensure they lie within acceptable ranges for resonance avoidance. The eigenfrequency check is outside the scope of this article, but is an additional constraint that, in parallel to the other structural checks, must be satisfied by the design. The eigenanalysis can be performed by calculating cross-sectional inertial and stiffness properties and passing them to an ad-hoc finite-element analysis (FEA) module. Young's and shear moduli to be used by the FEA are the pure concrete ones, and the effective density ρ_{ceff} is calculated as in Eq. (20):

$$
\rho_{ceff} = \frac{\rho_c A_c + \rho_s A_{stot}}{A_g}
\tag{20}
$$

Table 1
Examples of SOFT4S's Geometry and Material Property Inputs

Input	Type	Description	Default Value	Units
ρ_c	parameter	concrete density	2300	$\mathrm{kg\,m^{-3}}$
E_c	parameter	concrete Young's modulus	38e3	MPa
f_c	parameter	concrete compressive strength	60	MPa
ρ_s	parameter	longitudinal reinforcement density	7850	$\mathrm{kg\,m^{-3}}$
E_s	parameter	longitudinal reinforcement Young's modulus	200e3	MPa
f_{ys}	parameter	longitudinal reinforcement yield strength	414	MPa
ν_s	parameter	longitudinal reinforcement Poisson's ratio	0.33	–
ρ_{st}	parameter	shear reinforcement density	7850	$\mathrm{kg\,m^{-3}}$
E_{st}	parameter	shear reinforcement Young's modulus	200e3	MPa
f_{yst}	parameter	stirrup/tie yield strength	276.0	MPa
ν_{st}	parameter	shear reinforcement Poisson's ratio	0.33	–
ρ_p	parameter	cable density	7805	$\mathrm{kg\,m^{-3}}$
E_p	parameter	cable steel Young's modulus	195e3	MPa
f_{yc}	parameter	cable yield strength	1062	MPa
ν_t	parameter	cable Poisson's ratio	0.33	–
f_{uc}	parameter	cable ultimate strength	1250	MPa
σ_{C1pt}	variable	normal (axial) stress in cable set $C1$ at pre-stressing	$0.7{*}A_{C1}{*}f_{yc}$	N
σ_{C2pt}	variable	normal (axial) stress in cable set $C2$ at pre-stressing	$0.7{*}A_{C2}{*}f_{yc}$	N
$n_{s,i}$	variable	number of non-prestressed, inner longitudinal reinforcement	>8	–
$n_{s,o}$	variable	number of non-prestressed, outer longitudinal reinforcement	>8	–
$D_{s,i}$	variable	inner longitudinal-reinforcement placement diameter	–	m
$D_{s,o}$	variable	outer longitudinal-reinforcement placement diameter	–	m
$d_{s,i}$	variable	inner longitudinal-reinforcement diameter	–	m
$d_{s,o}$	variable	outer longitudinal-reinforcement diameter	–	m
s_{st}	variable	shear reinforcement (spiral/tie) pitch or spacing	–	m
s_{sv}	variable	shear reinforcement (spiral/tie) spacing	–	m
$D_{ss,i}$	variable	inner shear-tie placement diameter	$d_L+2c_c+d_{ssi}$	m
$D_{ss,o}$	variable	outer shear-tie placement diameter	$D_L-2c_c-d_{sso}$	m
d_{ssi}	variable	inner shear-tie diameter	–	m
d_{sso}	variable	outer shear-tie diameter	–	m
D_L	variable	leg outer diameter	–	m
d_L	variable	leg inner diameter	–	m

where ρ_c is the concrete density; A_c is the pure concrete cross-sectional surface area; ρ_s is the longitudinal reinforcement density; A_{stot} is the total nonprestressed reinforcement cross-sectional area at the station of interest; A_g is the gross cross-sectional area.

The main assumptions made in the leg dimensioning process described in this paper are:

1. The leg cross-section is assumed constant along the leg span. This arrangement streamlines formwork and manufacturing. As will be shown, the middle-span is the most stressed cross-section, hence tapering would have to be realized from the leg center toward the ends, and the resulting mass advantage at this point is not deemed significant. For the same reason, the numbers and sizes of non-prestressing reinforcement could theoretically change from section to section, but this is beyond the scope of this study.

2. The tensile strength of the concrete is assumed nil.
3. The generic cross-section is considered uncracked at SLS, but it is allowed to crack beyond that load level and at ULS. When the load reduces below the SLS level, the crack would close and the leg would retain the necessary integrity and dynamic properties of an uncracked structure.

Under those assumptions, and with reference to Fig. 3 and Fig. 8, the leg's geometry and structural properties are fully determined by:

- outer and inner diameters (D_L, d_L);

- the number and size of prestressing, stay cables;

- the number and size of nonprestressing reinforcement;

- the number and size of shear reinforcement (ties, hoops, or spirals);

- material properties (as shown, for example, in Table 1).

The structural verification process of a prestressed concrete (PSC) leg design of given geometry and parameters as in Table 1 starts with the identification of SLS, FLS, and ULS loads.

The SLS loads can be conservatively taken as those at 'quasi-steady-state', with rated conditions and severe sea state (e.g., design load case (DLC) 1.6 IEC, 2019). Extreme sea-states with faults (e.g., DLC 6.2 IEC, 2019), extrapolated loads with return periods of once every 50 yr from DLC 1.1, or other emergency cases may give rise to the ULS loads. FLS loads can be extracted from normal power production and parked/idling cases (e.g., DLC 1.2 and 6.4 IEC, 2019). These loads can be derived through dedicated AHSE simulations.

The key steps for SLS and ULS verification are listed below:

1. Determine external loads via AHSE and post-processing of results.
2. Calculate cross-section normalized area and second area moments of inertia.
3. Calculate eigenfrequencies and ensure they are within tolerances.
4. SLS verification
   (a) Calculate internal loads solving Eq. (17), which also accounts for second order effects and moment amplification due to bending deflection. In the vertical plane, a conservative value of the resultant of the gravitational, inertial, and hydrodynamic distributed loads can be employed as mentioned in Section 3. The lateral plane loads are not explicitly treated in this article, but are verified in SOFT4S in a similar manner. The resultant internal loads in this document are denoted by: N (axial load at the span station of interest, negative if compressive), M bending moment about the local x_b axis at the span station of interest, M_z (torque at the span station of interest), and T (shear component along the y-axis at span station of interest). In Fig. 9, the local reference frame is shown with the typical leg cross-section, with the x-axis aligned with the resultant bending moment M, and therefore the y-axis is normal to the neutral axis.
   (b) Ensure maximum cable prestress value below allowable (e.g., $\sigma_{C1pt}, \sigma_{C2pt} < A_{C1}, A_{C2} \times 0.7 f_{uc}$) ACI, 2014, Section 20.3.2.5) or per cable vendor recommendations; f_{uc} is the cable ultimate strength.
   (c) Ensure maximum acceptable leg tip deflection against an adequate threshold, for example one that would guarantee a safe margin from the slack condition of $C2$.
   (d) Ensure quantities of longitudinal and shear reinforcement are adequate to satisfy design standards (e.g., ACI, 2014).
   (e) Verify the stresses in the cross-sections of interest against SLS per section 5.1.1. Additionally, ensure longitudinal and shear reinforcement is adequate to satisfy spacing requirements by ACI (2014). This verification will also lead to the sizing of cable pre-tension, cable cross-sectional area, concrete, and non-prestressed reinforcement.
5. ULS verification
   (a) As for the SLS, calculate the internal loads for ULS. For simplicity, the resultant loads are still denoted by the same symbols as for the SLS load case (N, M, M_z, and v).
   (b) Verify the strength of the cross-sections of interest against ULS per section 5.1.2

Note that the SOFT4S code calculates all the geometric and inertial properties for a cross-section defined as in Fig. 8, including the area first and second moments of inertia and centroids of the individual reinforcement groups and with respect to an axis of symmetry (say the x axis) or to a calculated chord location (e.g., above the cross-section neutral axis).

5.1. Verification of PSC Leg Cross-Section and Cable Cross-sections

The assumed cross-section of the PSC leg and its main (x, y) coordinate system with origin in the geometric center are depicted in Fig. 8. The meaning of the other symbols are given in Table 1 and in the following Sections.
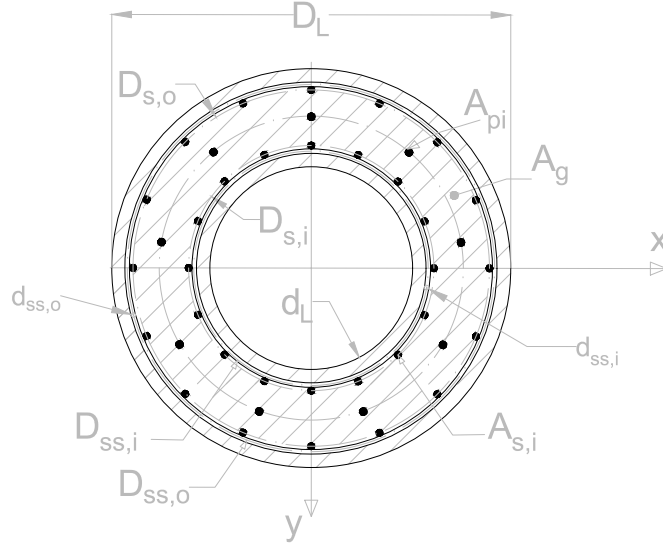

Figure 8: SF's leg typical horizontal cross-section and main geometry item definitions. Reinforcement symbols: D_L denotes the leg outer diameter; d_L denotes the leg inner diameter; A_g denotes the gross cross-sectional area; $D_{s,o}$ ($D_{s,i}$) denotes the outer (inner) longitudinal-reinforcement placement diameter; d_{sso} (d_{ssi}) denotes the outer (inner) shear-tie diameter; $D_{ss,o}$ ($D_{ss,i}$) denotes the outer (inner) shear-tie placement diameter; $A_{s,i}$ denotes the nonprestressed reinforcement cross-sectional area; $A_{p,i}$ denotes the prestressing tendon cross-sectional area (note: tendons are shown for completeness, but are unused in the actual design of the SF leg).

5.1.1. Verification against SLS limit states

At SLS, the cross-section is considered uncracked, therefore, with reference to Fig. 9, the neutral axis position must satisfy the condition:

$$y_n \geq D_L/2 \tag{21}$$

where y_n is the neutral axis distance from the cross-section's centroid. Here the goal is to find the number and size of cables and the associated prestress levels necessary to guarantee minimum deflection and uncracked conditions of the leg. The optimal design condition is to have the bottom fiber in Fig. 9 at 0-strain when the SLS load set is applied. The strain in the concrete, $\epsilon_c(y)$, can be expressed as a function of Y_G as shown in Eq. (22):

$$\frac{\epsilon_c(y)}{y_n - y} = \frac{\epsilon_{c,min}}{h_n} \tag{22}$$

where h_n is the neutral axis distance from the cross-section extreme compressed fiber; and $\epsilon_{c,min}$ is the minimum strain in the concrete.

If we ignore the nonlinearity between stress and strain, as commonly done in SLS verifications, and leverage the uncracked condition and symmetry of the cross-section, then the normalized cross-sectional area and second area moment (i.e., $A_{c,eff}$ and J_{xxceff}, Gilbert and Mickleborough, 2004; MacGregor, 2011) can be used to calculate the normal compressive stresses in the concrete (σ_{cz}) as in Eq. (23):

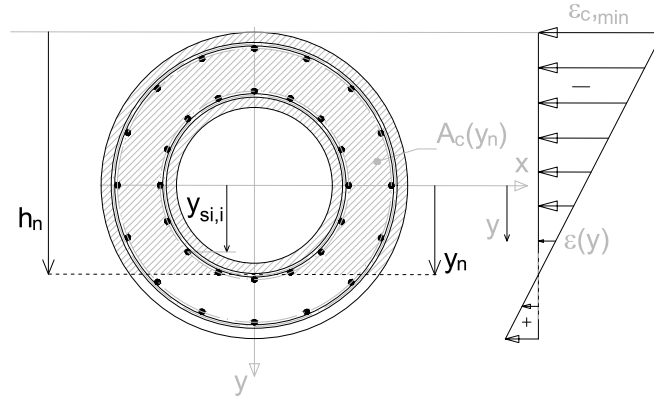$$\sigma_{cz} = \gamma_{f,sls} \left[\frac{N}{A_{c,eff}} + \frac{M}{J_{xxceff}} y \right] \tag{23}$$

Figure 9: Typical strain distribution (ϵ) under axial and flexural loads for a typical leg's cross-section. Symbols: h_n is the neutral axis distance from the cross-section extreme compressed fiber, and that corresponds to the coordinate y_n; $y_{s,i}$ is the y-coordinate of i-th rebar element; $A_c(y_n)$ is the pure concrete cross-sectional surface area above the chord at y_n; $\epsilon_{c,min}$ is the minimum strain in the concrete.

where $\gamma_{f,sls}$ is the load partial safety factor for SLS. For the generic rebar located at y_s, assuming perfect bonding of rebar and concrete, one could attain the compressive stress as in Eq. (24):

$$\sigma_{sz}(y_s) = \sigma_{cz}(y_s)nRC \tag{24}$$

where nRC is the ratio of rebar steel to concrete Young's moduli.

Once the stresses and strains are known, the criteria indicated in Appendix E must be met per ACI (2014).

5.1.2. Verification against ULS limit states

At ULS, the cross-section is assumed to have reached the maximum compressive strain in the concrete, and possibly cracked in the tension zone. The verification consists of ensuring that the ultimate strength of the cross-section is adequate for the ultimate loading conditions. In the case of the leg, a slender member subject to axial and flexure loading, stability is obviously a possible failure. The model developed in Sections 3–4 implicitly included second order effects, however. Hence, here, it will be sufficient to concentrate on the cross-section ULS design as would be done for a 'short' member. ACI (2014) requires:

$$\phi_{ACI}P_n \geq N_u \tag{25}$$
$$\phi_{ACI}M_n \geq M_u \tag{26}$$
$$\phi_{ACI}V_n \geq T_u \tag{27}$$
$$\phi_{ACI}T_{qn} \geq M_{zu} \tag{28}$$

where P_n, N_u are the nominal axial strength in compression, for a given external bending moment, and factored normal (axial) load at the station of interest, respectively; M_n, M_u are the nominal bending moment resistance at the station of interest, and factored bending moment at the station of interest, respectively; V_n, T_u are the nominal shear strength at the station of interest, and factored shear load at the station of interest, respectively; and T_{qn}, M_{zu} are the nominal torsional strength, and factored torsion load at the station of interest, respectively. First, the axial and bending moment loads should be assessed against the design interaction curve, then other code check criteria can be verified.

In Fig. 10a, the assumed concrete strain distribution with a maximum compressive strain value equal to ϵ_{cu} and a stress distribution characterized by the stress block (Whitney, 1937; ACI, 2014, Sect. 22.2.2.4.1) are shown. For generality, the cross-section is shown with prestressed elements as well. It is not expected that these elements will be needed, given the pre-load coming from the stay cable, however. To extract the nominal cross-sectional strengths, the following force- and moment-balance system of equations (Eq. (29)) must be solved.

$$\begin{cases} N = C_c + T_{stot} + T_{ptot} \\ M_n = C_c Y_G|_{C_c} + T_{stot} Y_G|_{T_{stot}} + T_{ptot} Y_G|_{T_{ptot}} \end{cases} \tag{29}$$
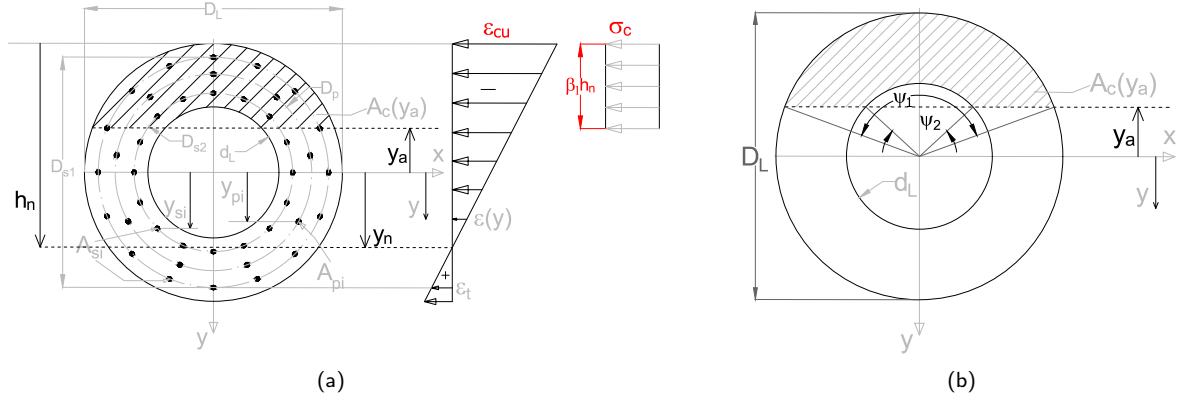
Figure 10: SF leg cross-section's strain and stress distributions under the stress-block assumption (a); and definition of circular-segment ψ_1 and ψ_2 angles associated with the chords at y_a (b).

where C_c is the resultant force in the compressive concrete part of the cross-section (negative if compressive) (see Eq. (30)); T_{stot} is the resultant force from the nonprestressed reinforcement (positive if tensile) (see Eq. (31)); T_{ptot} is the resultant force from the prestressed reinforcement (positive if tensile) (see Eq. (32)); $Y_G|_{C_c}$ is the y-coordinate of the centroid of the forces resulting in C_c; $Y_G|_{T_{stot}}$ is the y-coordinate of the centroid of the forces resulting in T_{stot}; $Y_G|_{T_{ptot}}$ is the y-coordinate of the centroid of the forces resulting in T_{ptot}. In Eq. (29), M has been replaced by the nominal flexural strengths (M_n), to readily provide the utilization as shown below (Eq. (74)).

$$C_c = \sigma_{cz}(y)A_c(y_a) \simeq -0.85 f_c A_c(y_a) \tag{30}$$

$$T_{stot} = \sum_{i=1}^{ns} E_{si} A_{s,i} \epsilon_{s,i} \tag{31}$$

$$T_{ptot} = \sum_{i=1}^{np} E_{pi} A_{p,i} \epsilon_{p,i} \tag{32}$$

In Eq. (30), C_c is limited to the stress-block of depth $a = \beta_1 h_n$ (corresponding to the coordinate y_a), where β_1 is the factor relating the depth of the equivalent rectangular compressive stress block to the depth of neutral axis (ACI, 2014, Sect. 22.2.2.4.1); $A_{s,i}$ is the nonprestressed reinforcement cross-sectional area; $\epsilon_c(y)$ is the strain in the concrete; $\epsilon_{s,i}$ is the strain in the i-th rebar; $\epsilon_{p,i}$ is the strain in the i-th prestressed tendon. In the above equations, the index i has been added to E_s, E_p for generality, though in most common applications those values will be constant for all i values.

For a hollow circular section (Fig. 10b), $A_c(y_a)$ can be written as in Eq. (33):

$$A_c(y_a) = \frac{D_L^2}{8}\left(\psi_1 - \sin(\psi_1)\right) - \frac{d_L^2}{8}\left(\psi_2 - \sin(\psi_2)\right) \tag{33a}$$

$$\psi_1 = 2\pi - 2\cos^{-1}\frac{2y_a}{D_L} \tag{33b}$$

$$\psi_2 = \begin{cases} 2\pi - 2\cos^{-1}\dfrac{2y_a}{d_L} & \text{if} \quad |y_a| < \dfrac{d_L}{2} \\[2mm] 0 & \text{if} \quad y_a < -\dfrac{d_L}{2} \\[2mm] 2\pi & \text{if} \quad y_a > \dfrac{d_L}{2} \end{cases} \tag{33c}$$

Analogously, $Y_G|_{C_c}$ can be calculated noting that for a circular segment Eq. (34) applies, and appropriately removing

the contribution from the inner circular segment if $y_a > -\dfrac{d_L}{2}$:

$$Y_G|_{A_c(y_a)} = -\frac{2}{3} \frac{D_L{}^3 \sin^3\left(\frac{\psi_1}{2}\right) - d_L{}^3 \sin^3\left(\frac{\psi_1}{2}\right)}{D_L{}^2 \left(\psi_1 - \sin(\psi_1)\right) - d_L{}^2 \left(\psi_2 - \sin(\psi_2)\right)} \tag{34}$$

Because it will be used later, we can also calculate the second area moment of inertia ($J_{xx}|_{A_c(y_a)}$):

$$J_{xx}|_{A_c(y_a)} = \frac{D_L{}^4}{128}\left(\psi_1 - \sin(\psi_1)\cos(\psi_1)\right) - \frac{d_L{}^4}{128}\left(\psi_2 - \sin(\psi_2)\cos(\psi_2)\right) \tag{35}$$

The generic $\epsilon_c(y)$ ($\epsilon_p(y)$) is calculated via Eq. (36):

$$
\begin{aligned}
\epsilon_c(y) &= \epsilon_{cu}\frac{h_n - D_L/2 - y}{h_n} \\
\epsilon_{s,i} = \epsilon_s(y_{s,i}) &= \epsilon_c(y_{s,i}) \\
\epsilon_{p,i} = \epsilon_p(y_{p,i}) &= \epsilon_{p0,i} + \hat{\epsilon}_{p,i}
\end{aligned}
\tag{36}
$$

with

$$\epsilon_{p0,i} = \frac{P_{0i}(1 - R_\infty)}{E_{pi} A_{p,i}} \tag{37}$$

$$\hat{\epsilon}_{p,i} = \epsilon_{cu}\frac{h_n - D_L/2 - y_{p,i}}{h_n} \tag{38}$$

where $\epsilon_{p0,i}$ is the strain in the i-th prestressed tendon due to prestress only; P_{0i} is the tendon initial prestress force (positive); $\hat{\epsilon}_{p,i}$ is the contribution to the i-th prestressed tendon strain due to bending in the cross-section; $A_{c,eff}$ is the effective (normalized) concrete cross-sectional surface area; R_∞ is the relaxation loss in percentage of initial preload; n_p is the number of prestressing tendons; $y_{s,i}$ is the y-coordinate of i-th rebar element; $y_{p,i}$ is the y-coordinate of i-th prestressed tendon element.

Note that the strain in the rebar ($\epsilon_s(y)$) is the same as $\epsilon_c(y)$, because the rebar is assumed fully bonded with the concrete. For the prestressing tendons, however, $\epsilon_p(y_{p,i})$ must account for the prestress strain and for the concrete compressive strain at transfer.

Finally the stresses in the reinforcement elements are calculated as Eq.s (39)–(40):

$$\sigma_{sz}(y_{s,i}) = \begin{cases} \text{sign}\left(\epsilon_s(y_{s,i})\right) f_{ys} & \text{if} & \left|E_s\epsilon_s(y_{s,i})\right| \geq f_{ys} \\ E_s\epsilon_s(y_{s,i}) & \text{otherwise} \end{cases} \tag{39}$$

$$\sigma_{pz}(y_{p,i}) = \begin{cases} \text{sign}\left(\epsilon_p(y_{p,i})\right) f_{yp} & \text{if} & \left|E_p\epsilon_p(y_{p,i})\right| \geq f_{yp} \\ E_p\epsilon_p(y_{p,i}) & \text{otherwise} \end{cases} \tag{40}$$

where $i = 1..n_{s,i}$ or $i = 1..n_{s,o}$ for either inner or outer circle reinforcement, respectively. Note that Eq. (40) can be readily replaced with a nonlinear function of the strain.

As can be easily observed, only one unknown exists, i.e., h_n, as all the other variables in the above equations are functions of h_n. By solving the first of Eq. (29) for a given value of the external axial load N, h_n can be determined. Corresponding to that neutral axis position, one could determine the additional external bending moment that the cross-section can withstand. Varying N from the maximum compressive strength ($P_{n,max}$, Eq. (41); per ACI, 2014, Section 22.4.2), to the maximum tensile strength ($P_{nt,max}$, Eq. (42); per ACI, 2014, Section 22.4.3), one could determine the associated M_n's, and compile an interaction diagram as shown in Fig. 15.

$$P_{n,max} = \left[0.85 f_c\left(A_g - A_{stot} - A_{ptot}\right) + f_{ys}A_{stot} - \left(f_{se} - 0.003 E_p\right)A_{ptot}\right] \begin{cases} 0.8 & \text{if tie shear reinforcement} \\ 0.85 & \text{if spiral shear reinforcement} \end{cases} \tag{41}$$

$$P_{nt,max} = f_{ys}A_{stot} + f_{se}A_{ptot} \tag{42}$$

where f_{se} is the stress in the prestressing reinforcement at nominal axial strength of the cross-section;

To complete the verification against ULS, the criteria listed in Section F must be met.
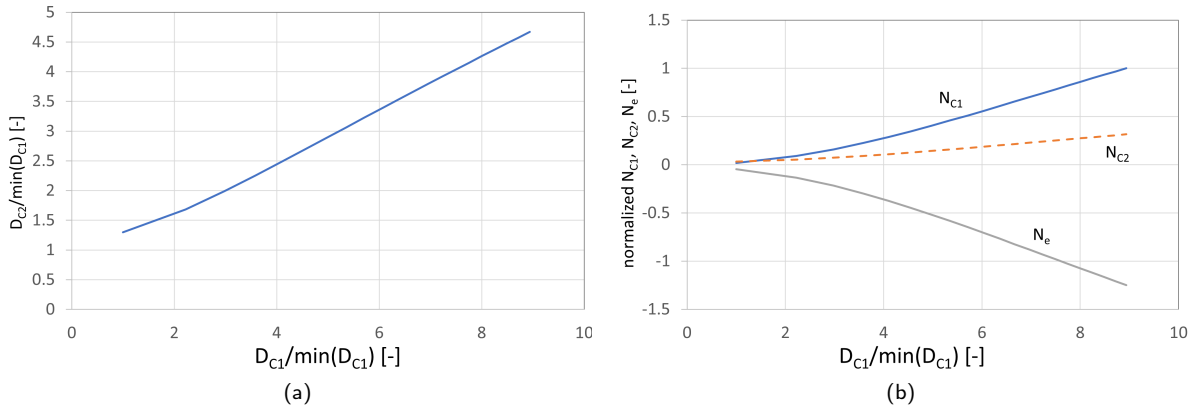
Figure 11: Results from SOFT4S's structural model in terms of: (a) cable $C2$ diameter vs. cable $C1$ diameter that allow for a nil vertical deflection at post-tensioning; and (b) cable tensions and leg load (aligned with $\overline{AB}$) at post-tensioning transfer as a function of $C1$ cable diameter. Cable diameters are normalized by the minimum examined $C1$ cable diameter, and loads (caret symbols) by the minimum $C1$ load.

6. Case Study and Model Cross Verification

In this section, we show the results of a preliminary design iteration for the SF leg and cable assembly based on expected overall footprint, mass, and required buoyancy to support a 10 MW turbine, and a generic 70 MPa-strength concrete. As the SF is covered by sensitive intellectual property (IP), we present normalized loads and geometry quantities from SOFT4S's results.

Two loading scenarios were considered: the first is representative of the load transfer at post-tensioning during the assembly phase on land, and the second represents the (quasi-) steady-state situation under operational conditions at sea. Typical values for effective buoyancy value and the horizontal component of the force exerted by the can and mooring line onto the leg during operation were derived through dedicated fully-coupled AHSE simulations. On dry-land, the only external loads considered are due to gravitational effects, both distributed along the leg span and concentrated at the joints.

The method described in Section 3 was used to arrive at the internal loads for cables and legs. First, a sensitivity analysis of cable cross-section is given in Fig. 11a. In this graph, the upper cable diameter is shown as a function of the lower cable counterpart, under the assumption that no vertical deflection w is permitted at post-tensioning transfer, and with cable pre-tensioning loads equal to $P_{0,c1} = \sigma_{C1pt}A_{C1}$ and $P_{0,c2} = \sigma_{C2pt}A_{C2}$, for lower and upper cable, respectively. In Fig. 11a, the diameters are normalized by the minimum value considered for $C1$. The upper cable is considerably less loaded than the lower cable, due to the geometry and the difference between the angles θ_{C1} and θ_{C2}, and this also translates in a relatively insensitive variation of the $C2$ diameter with respect to the size of $C1$. Note, in fact, that increasing A_{C1}, for a given pre-tensioning stress, is equivalent to increasing both the leg axial load as well as the tension in the upper cable, which then requires a larger cross-section for the imposed strength constraints. The increase in upper- over lower-cable diameter, however, is proportional to a 1:2 ratio. This contributes to keeping the elevation of the substructure center-of-mass relatively low with obvious advantages on stability, but at the price of higher load demand on the lower cable and leg. Alternatively, the leg-to-stem joint could be designed at a higher elevation than that leg-to-can joint. This optimization is outside the scope of this study however.

Fig. 11b shows that the component of the leg axial load aligned with $\overline{AB}$ (N_e) increases more than the individual cable tensions as the cable size increases. To fix a set of cable dimensions, more analyses on the dynamic characteristics of the system should be performed, for example to guarantee avoidance of modal frequencies that can lead to dangerous resonance. Here, for sake of brevity, we determined the size of the cables based on an acceptable mean leg-tip deflection of 0.2 m at rated conditions and with normal sea-state (significant wave height of 1.13 m, 7.22 s peak spectral period).

In Fig. 12a, the leg tip deflections and the loads in the leg and cables are shown as functions of the normalized can buoyancy. To note is a sharp variation in the deflection occurring when the external load actions exceed a value of approximately 1.35 the mean buoyancy. In that situation, in fact, the upper cable becomes slack (Fig. 12b) and the
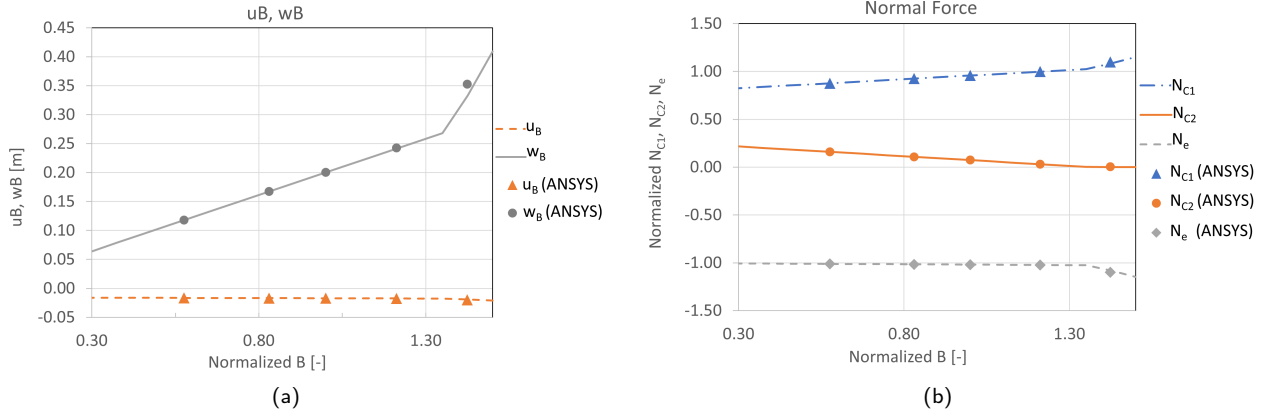
Figure 12: Results from SOFT4S's structural model and ANSYS in terms of: (a) leg tip deflections (horizontal and vertical, u_B, w_B) as a function of effective buoyancy load magnitude; and (b) cable and leg loads (normalized by the maximum N_{C1}) as a function of can buoyancy load. Buoyancy values are normalized by the can mean buoyancy calculated in the assumed operational conditions.
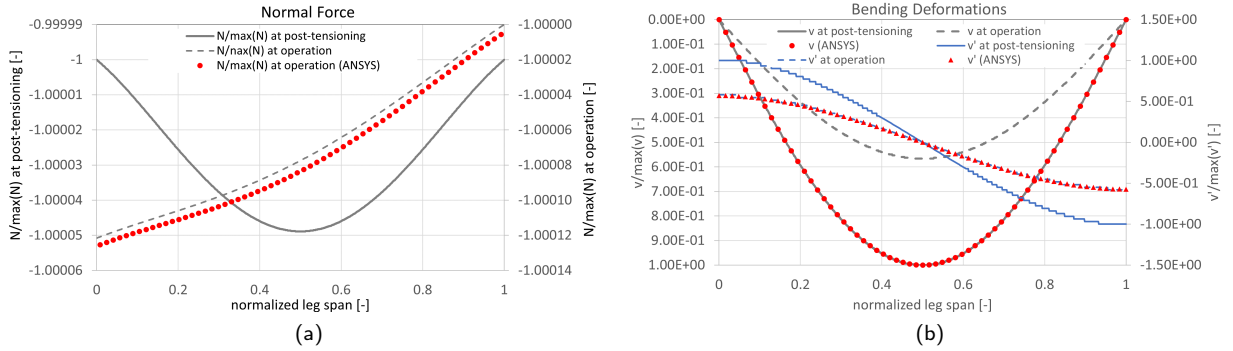

Figure 13: Results from SOFT4S's structural model and ANSYS in terms of normal loads (a) and leg axis deflection and cross-section rotation (b). Results are normalized by the maximum loads and deflections from the post-tensioning case.

overall system may fail. Although not necessarily representing a chosen layout, the present case study is an example of how the design method can be used to assess safety margins with respect to stability conditions for the entire system. Changes in the design, for example by selecting a cable layout with higher pre-tension, or further limiting the leg tip deflection under operational conditions, could guarantee a larger margin of safety with respect to cable slackness.

Turning now to the design of the leg cross-section, Fig. 13 shows the leg's normal loads, and the translational and rotational deflections along the span for the two load cases considered herein. As seen from the graphs, SOFT4S's nonlinear elastic beam method can account for bending brought forth by second-order effects, and the variation of the normal load as a function of span due to the transverse deflection. At post-tensioning transfer, the leg maximum deflection occurs at mid-span, and it is approximately double the mean deflection calculated at operation. At sea, the component of the distributed weight along the leg axis is non-nil due to the inclination of the leg, and therefore the largest axial load is registered at the joint with the central stem.

SOFT4S-calculated internal shear and bending moments are presented in Fig. 14. The largest shear values are found at the leg ends, whereas the maximum bending moments occur at mid-span for both loading scenarios. The at-sea case renders about half the internal load magnitudes than those at post-tensioning transfer. Again, this emphasizes how the assembly and the post-tensioning of the SF are critical aspects of both the structural analysis and of the actual construction phases.

The cross-section verification against SLS and ULS was conducted by conservatively assuming that the maximum
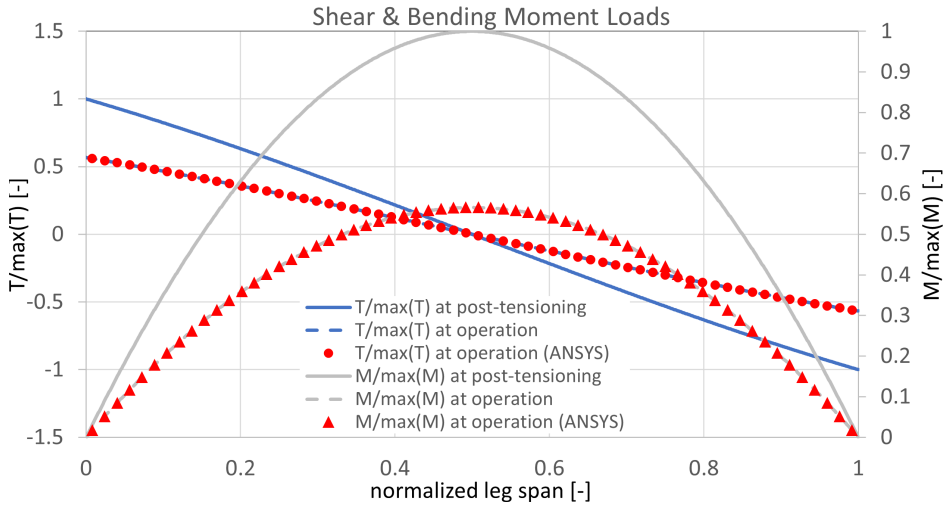
Figure 14: Results from SOFT4S's structural model and ANSYS in terms of internal shear and bending moment loads along the leg span (0 is at the *A* and 1 at the *B* joint). Results are normalized by the respective load maxima.

shear acts together with the maximum bending moment and normal load at the mid-span station. The arrangement of the reinforcement is as in Fig. 9. For the mid-span location, a ULS interaction diagram was compiled and the results are shown in Fig. 15. The curves represent the capacity (baseline and factored per (ACI, 2014)) of the optimized (minimum mass) cross-section, and the markers denote the two loading conditions analyzed in this example. The post-tensioning
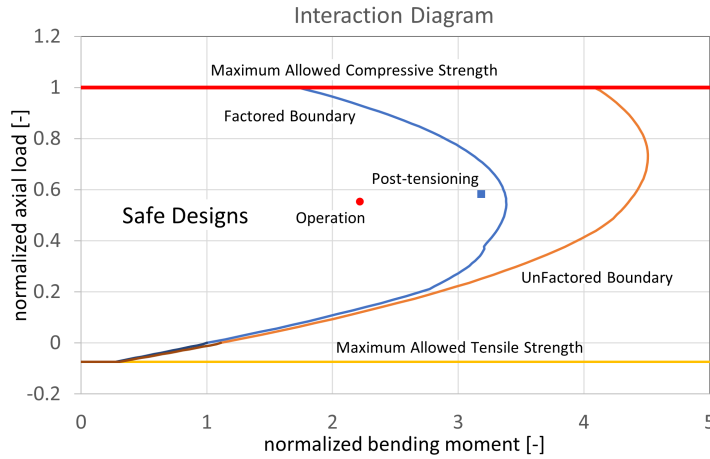
Figure 15: Calculated interaction diagram. The curves represent the ultimate capacity of the leg cross-section. The two points represent the conditions at post-tensioning transfer (blue square) and at operational steady-state (red circle) (factored for ULS $\gamma_{f,uls}$)

.

load-transfer scenario is the design driving case, and the associated factored loads are just within the acceptable safe boundaries leading to a well balanced design. The remainder safety margin ($\sim 5\%$) will account for additional effects unknown at preliminary design.

The component mass was calculated at some 27 t for the cables and 270 t for the leg including reinforcement. With preliminary estimates on buoyancy-can and stem masses, we project the total structural mass of the SF at approximately 2000 t. Although this is a preliminary outcome, it shows how the SF departs from heavier conventional designs (e.g., PPI's steel WindFloat at approximately 2400 tonne for an 8 MW turbine (Banister, 2018); Ideol's concrete FloatGen at

4000 t and 8250 t for a 2 MW[2] and a 6 MW turbine (Choisnet et al., 2016), respectively; University of Maine's concrete VolturnUS at 11,200 t for a 6 MW turbine (Allen, 2019).)

The results shown in this Section were cross-verified with a dedicated FEA in ANSYS Mechanical APDL Release 2019 R2, commercial FEA package to prove the validity of the newly devised analytical model. The leg was assumed as made out of an equivalent isotropic material with Young's modulus equal to E_c and a concrete effective density as discussed above, further modified for distributed buoyancy effects. The beam was simulated with a set of *beam188* elements (more than one to better capture the deformed shape), whereas the cables were discretized with a series of *link180* subjected to a pretension proportional to their cross-sectional areas. Data extracted from ANSYS runs (Fig.s 12–14, Fig. 16)) exhibited excellent agreement with results from SOFT4S in terms of both internal loads and deflections. In Fig. 16, we report ANSYS plots of the calculated nodal displacement w, the normalized axial force in cables and legs, and the bending moment in the leg for the studied operational case. For completeness, an eigenfrequency analysis was performed to assess the first few structural modes. The first mode (1.94 Hz) is in the lateral plane, whereas the first mode in the vertical plane showed a frequency of 3.68 Hz (see Fig. 16d).

The shape functions in ANSYS's beam element do not readily capture the second-order effect that our new method includes, and the FEA had to be carried out in a fully nonlinear fashion to achieve results. Whereas ANSYS requires only a few seconds to solve the analysis (versus SOFT4S's less than 1 s on a modern Intel 7 CPU), it also requires lengthier set-up and post-processing activities, and does not lend itself to an expedited integration with gradient-based optimization. SOFT4S, on the other hand, facilitates the expedited design of experiments and allows for a full exploration of the sensitivity to design variables and constraint parameters. More importantly, SOFT4S's analytical nature promotes a thorough understanding of the physics involved and guides the designers toward a more efficient optimization reducing risk to the project.

7. Conclusions and Future Work

The floating substructure and mooring components comprise about one third of the capital expenditure (CapEx) of a typical floating offshore wind power plant and are responsible for ∼20% of the LCOE (Stehly and Beiter, 2019). Reducing the cost of the floating platform can therefore greatly influence the final commercial viability of floating offshore wind. The SF was conceived to reduce these costs via a modularized slender structure, an efficient load path, an effective use of materials leveraging established concrete supply chain, and an industrialized approach to manufacturing. The structural design of the SF must both guarantee component reliability as well as floater stability.

In this paper, we developed a new analytical model to size both the leg and the stay cables, key components of the SF. The employed nonlinear, second-order method is capable of accounting for beam shortening due to bending and second-order bending due to compression. As such, this method inherently includes design and analyses against buckling instability. The method is implemented in SOFT4S, a tool for the optimization of the SF that includes hydrodynamic requirements, CCD inputs, and a cost model. Together with this new analytical beam theory, the steps necessary for the qualification and verification of the RC leg cross-section were presented primarily following ACI (2014). The SLS and ULS verifications were the focus of this study, although FLS will be analyzed following FIB (2013) and ECS (2004) once a complete load spectrum is captured by appropriate AHSE simulations that are being carried out within the ATLANTIS USFLOWT project. The newly devised method will serve as the main design and analysis tool to extract DELs and DESs.

The majority of the leg loading originates from the cable tensions, concentrated buoyancy thrust at the joint with the can, and distributed buoyancy along the leg span. Transverse hydrodynamic loading and other components in the vertical plane (e.g., viscous drag or inertial actions) are orders of magnitude smaller, as based on the preliminary results of AHSE simulations. Additionally, the listing angle of the SF is limited to ∼ ±10 deg. For these reasons, and for added clarity, the analysis was limited to the vertical plane statics, without losing in generality, with an obvious extension to the transverse statics.

A case study was provided to prove the capability of SOFT4S's structural model. Two loading situations were analyzed: the load transfer at post-tensioning, and the at-sea, operational quasi-steady-state loading scenario. First, the results of the model helped select the cable size for a prescribed mean leg tip deflection. Then, the returned internal loads were used to size the cross-section and its reinforcement. The data demonstrate that SOFT4S is capable of optimizing the cross-section of the leg and cables given the constraints discussed in Section 5.1, while also guaranteeing

---

[2]https://www.mre-paysdelaloire.com/news/the-floatgen-floating-wind-turbine-at-a-new-operational-stage/ accessed 11/2020
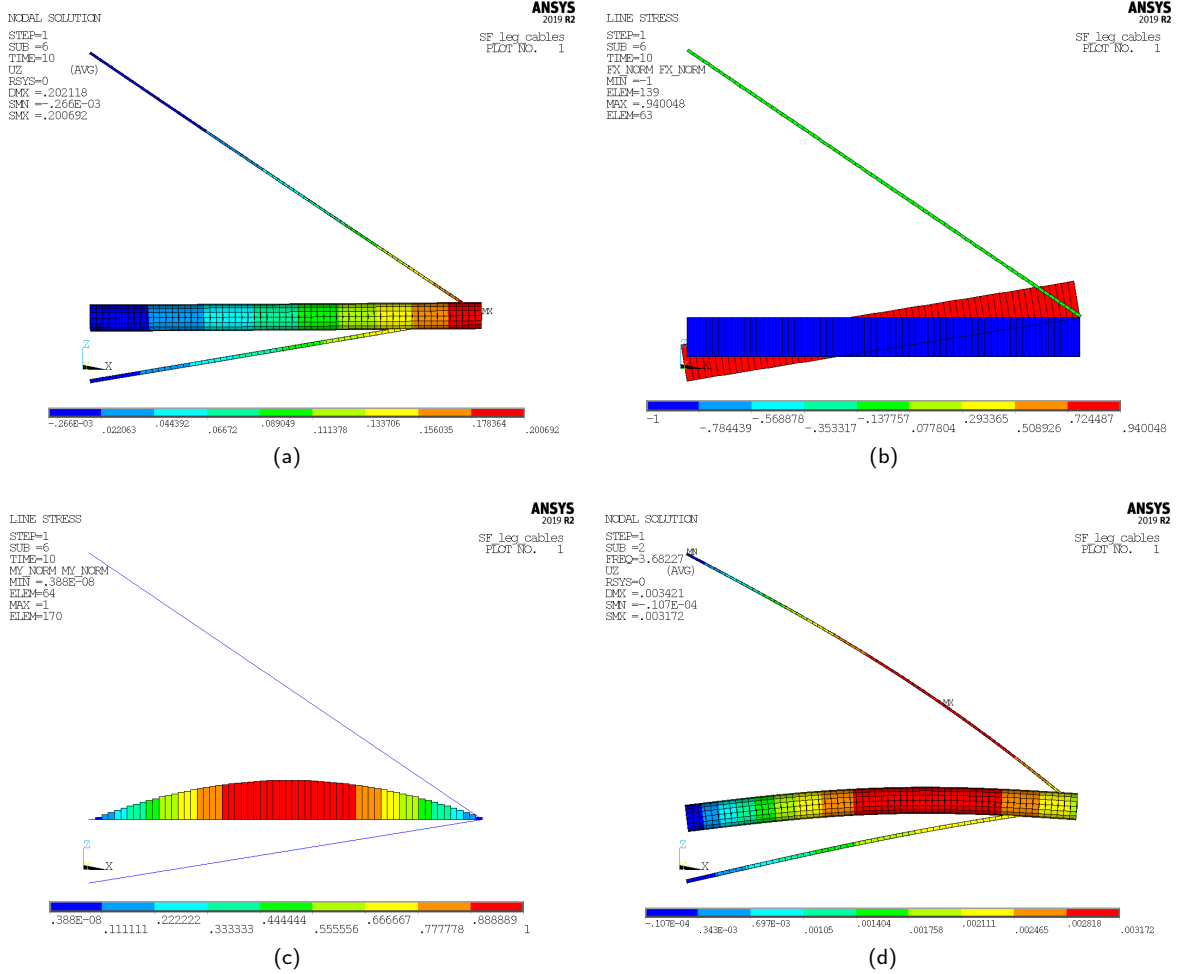
Figure 16: Results from a dedicated ANSYS FEA showing the vertical component of the deflection w (a), the axial force (b), and the bending moment (c) normalized by the respective maxima calculated in the leg; and (d) the second eigenmode shape.

hydrostatic stability of the floater and other hydrodynamic performance parameters that will be discussed in a separate paper. The model is computationally efficient and sensitivity analyses for assessing trade-offs between structural mass and control demand to safeguard floater stability and performance can be performed with negligible impact on the design process timeline.

A cross-verification against the commercial package ANSYS showed excellent agreement in the results of the static load and deformation analysis. It is important to note that element shape functions in commercial FEM software typically miss the second-order effects that SOFT4S's beam model encompasses, and require multiple nonlinear runs to reach the same results.

The model is now being extended to the central stem of the SF and, with some modifications, to the buoyancy cans. Additionally, we are planning to include a modal analysis capability that will help identify viable designs against frequency acceptance bands. When complete, SOFT4S will then render mass or cost optimized configurations of cables, central stem, and legs, for given environmental conditions, control system and turbine parameters.

A. List of Acronyms

ABS American Bureau of Shipping
AHSE Aero-hydro-servo-elastic
ALS Accidental limit states
ARPA-E Advanced Research Projects Agency-Energy
ATLANTIS Aerodynamic Turbines Lighter and Afloat with Nautical Technologies and Integrated Servo-control

CapEx Capital expenditure
CCD Control co-design
CSM Colorado School of Mines
CU University of Colorado at Boulder

DEL Damage equivalent load
DES Damage equivalent stress
DLC Design load case
DOE Department of Energy
DOF Degree of freedom

FEA Finite-element analysis
FEM Finite-element method
FLS Fatigue limit state
FOWT Floating offshore wind turbine

GFRP Glass-fiber reinforced plastic

IP Intellectual property

LCOE Levelized cost of energy

NREL National Renewable Energy Laboratory

O&G Oil and gas
ODE Ordinary differential equation

PDE Partial differential equation
PSC Prestressed concrete

RC Reinforced concrete

SF SpiderFLOAT
SLS Serviceability limit state
SOFT4S SpiderFLOAT Offshore Floater Tool for Sizing

ULS Ultimate limit state
USFLOWT Ultra-flexible Smart Floating Offshore Wind Turbine
UVA University of Virgina

B. List of Symbols

ANSYS ANSYS Mechanical APDL Release 2019 R2, commercial FEA package

a Depth of stress-block from top compressed fiber
a_c Generic constant
$\underline{a}$ Generic constant
$\overline{a}$ Generic constant
A Joint between leg and central stem
$\overline{AB}$ Line connecting A to B
A_c Pure concrete cross-sectional surface area
$A_{c,eff}$ Effective (normalized) concrete cross-sectional surface area
A_{cp} Area enclosed by outside perimeter of concrete cross section
A_{ct} Area of that part of the cross section between the flexural tension face and the centroid of the gross section
$A_c(y_a)$ Pure concrete cross-sectional surface area above the chord at y_a
$A_c(y_n)$ Pure concrete cross-sectional surface area above the chord at y_n
A_{C1} Cross-sectional area of cable set $C1$
A_{C2} Cross-sectional area of cable set $C2$
A_g Gross cross-sectional area
A_l Torsional additional longitudinal reinforcement total cross-sectional area

A_{Leff} Concrete, leg cross-sectional area normalized for nonprestressed rebar
A_o Area enclosed by the shear (spiral/tie) flow path
A_{oh} Area enclosed by centerline of shear (spiral/tie) reinforcement
$A_{p,i}$ Tendon cross-sectional area
A_{ptot} Total cable cross-sectional area at the station of interest
A_s Nonprestressed reinforcement cross-sectional area
$A_{s,i}$ Nonprestressed reinforcement cross-sectional area
A_{st} Shear reinforcement (spiral/tie) cross-sectional area
A_{stot} Total nonprestressed reinforcement cross-sectional area at the station of interest
A_v Torsional shear reinforcement (spiral/tie) cross-sectional area
A_{vtot} Total shear reinforcement cross-sectional area at the station of interest

b_c Generic constant
B Joint between leg and buoyancy can
$\mathbf{B_c}$ Buoyancy force at B
B_{eff} Effective buoyancy magnitude at joint B, accounting for other hydrodynamic forces, for the weight of the buoyancy can bundle, half the weight of the cables, and half the weight of the leg
$\mathbf{B_{eff}}$ Effective buoyancy at joint B, accounting for other hydrodynamic forces and the weight of the

buoyancy can bundle, half the weight of the cables, and half the weight of the leg

B_0 Joint between leg and buoyancy can undeflected conditions

c_c Concrete cover

c_1 Generic onstant used in the integration of ODE

c_2 Generic onstant used in the integration of ODE

C_c Resultant force in the compressive concrete part of the cross-section (negative if compressive)

$C1$ Cable set 1

$C1_a$ Cable 1a, one of the two cables in the $C1$ set

$C1_b$ Cable 1b, one of the two cables in the $C1$ set

$C2$ Cable set 2

$C2_a$ Cable 2a, one of the two cables in the $C2$ set

$C2_b$ Cable 2b, one of the two cables in the $C2$ set

d_c Single buoyancy can inner diameter

d_L Leg inner diameter

d_{sh} Distance to the center of pre and non-prestressed tension reinforcement from top fiber, but $\leq 0.8h_b$

$d_{s,i}$ Inner longitudinal-reinforcement diameter

$d_{s,o}$ Outer longitudinal-reinforcement diameter

d_{ssi} Inner shear-tie diameter

d_{sso} Outer shear-tie diameter

D_c Single buoyancy can outer diameter

D_L Leg outer diameter

$D_{s,i}$ Inner longitudinal-reinforcement placement diameter

$D_{s,o}$ Outer longitudinal-reinforcement placement diameter

$D_{ss,i}$ Inner shear-tie placement diameter

$D_{ss,o}$ Outer shear-tie placement diameter

E_c Concrete Young's modulus

E_p Cable steel Young's modulus

E_s Longitudinal reinforcement Young's modulus

E_{st} Shear reinforcement Young's modulus

f Generic continuos function

f_c Concrete compressive strength

f_r Rupture modulus

f_{se} Stress in the prestressing reinforcement at nominal axial strength of the cross-section

f_{uc} Cable ultimate strength

f_{up} Prestressing tendon ultimate strength

f_{us} Longitudinal reinforcement ultimate strength

f_{yc} Cable yield strength

f_{yl} Torsional longitudinal reinforcement yield strength

f_{yp} Prestressing tendon yield strength

f_{ys} Longitudinal reinforcement yield strength

f_{yst} Stirrup/tie yield strength

F_c Horizontal component of the force exerted by the can and mooring line onto the leg

g Magnitude of the gravitational acceleration

h_b Height/depth of the cross-section

h_n Neutral axis distance from the cross-section extreme compressed fiber

i_c Generic integer number

J_{xxceff} Normalized concrete cross-sectional second area moment of inertia

J_{xxg} Gross cross-sectional second area moment of inertia

$J_{xx}|_{A_c(y_a)}$ Second area moment of inertia for $A_c(y_a)$

$L_{C1,f}$ Cable $C1$ length with deformed geometry

$L_{C1,0}$ Cable $C1$ length with undeformed geometry

$L_{C2,f}$ Cable $C2$ length with deformed geometry

$L_{C2,0}$ Cable $C2$ length with undeformed geometry

L_L Leg length in the deformed condition

L_{L0} Leg length in the undeformed condition

m_{eff} Effective mass per unit length, to account for hydrostatic buoyancy, hydrodynamic, and distributed inertial loads

M Bending moment about the local x_b axis at the span station of interest

$\bar{M}$ Sum of M_C and one half the sum of M_{C1}, M_{C2}, and leg mass

M_{cr} Bending moment causing cracking at the cross-section of interest

M_C Mass of the buoyancy can bundle at B

M_{C1} Mass of cable set $C1$

M_{C2} Mass of cable set $C2$

M_n Nominal bending moment resistance at the station of interest

M_u Factored bending moment at the station of interest

M_z Torque at the span station of interest

M_{zu} Factored torsion load at the station of interest

n_m Number of members

n_p Number of prestressing tendons

nRC Ratio of rebar steel to concrete Young's moduli

$n_{s,i}$ Number of non-prestressed, inner longitudinal reinforcement

$n_{s,o}$ Number of non-prestressed, outer longitudinal reinforcement

N Axial load at the span station of interest

N_{C1} Normal force in cable $C1$

N_{C2} Normal force in cable $C2$

N_e Force exerted on the leg directed along the line connecting hinges $\overline{AB}$

$N_{e,cr}$ Eulerian critical load

N_u Factored normal (axial) load at the station of interest

p_h Perimeter described by centerline of stirrup element

$p(z_b)$ Component of the external, distributed static loading along the beam z_b axis

P_n Nominal axial strength in compression, for a given external bending moment

P_n^* Nominal axial strength, in either tension or compression depending on the N sign

$P_{n,max}$ Maximum nominal axial strength in compression

$P_{nt,max}$ Maximum nominal axial strength in tension

$P_{0,c1}$ $C1$ cable initial prestress force (positive)

$P_{0,c2}$ $C2$ cable initial prestress force (positive)

P_{0i} Tendon initial prestress force (positive)

$q(z_b)$ Component of the external, distributed static loading along the beam y_b axis

rx Factor for prestress long term relaxation

R_∞ Relaxation loss in percentage of initial preload

s_{st} Shear reinforcement (spiral/tie) pitch or spacing

s_{sv} Shear reinforcement (spiral/tie) spacing

t_w Wall thickness

T Shear component along the y-axis at span station of interest

T_{ptot} Resultant force from the prestressed reinforcement (positive if tensile)

T_{stot} Resultant force from the nonprestressed reinforcement (positive if tensile)

T_{qn} Nominal torsional strength

T_u Factored shear load at the station of interest

u_B Deflection of B along X_G

v Deflection normal to beam axis in the y_b direction

v' First derivative of v with respect to z_b

v'' Second derivative of v with respect to z_b

v''' Third derivative of v with respect to z_b

v_h Solution to the homogeneous ODE for v

v_p Particular solution to the ODE for v

V_c Concrete shear strength

V_n Nominal shear strength at the station of interest

V_s Shear strength due to tie/spiral reinforcement

w Deflection along beam axis in the z_b direction

w' First derivative of w with respect to z_b

w_B Deflection of B along Z_G

x Cross-section x-axis

x_b Beam local x-axis

X_G Global x-axis

y Cross-section y-axis

y_a Distance from cross-section centroid to bottom of stress-block

y_b Beam local y-axis

y_n Neutral axis distance from the cross-section's centroid

$y_{p,i}$ Y-coordinate of i-th prestressed tendon element

y_s Rebar element coordinate along y-axis

$y_{s,i}$ Y-coordinate of i-th rebar element

Y_G Global y-axis

$Y_G|_{A_c(y_a)}$ Y-coordinate of the centroid of $A_c(y_a)$

$Y_G|_{C_c}$ Y-coordinate of the centroid of the forces resulting in C_c

$Y_G|_{T_{ptot}}$ Y-coordinate of the centroid of the forces resulting in T_{ptot}

$Y_G|_{T_{stot}}$ Y-coordinate of the centroid of the forces resulting in T_{stot}

z_b Local z-axis

$\hat{z}_b$ Generic value of z_b

z_m Generic value of z_b

Z_G Global z-axis

C. List of Greek Symbols

α Constant in the solution of ODE

α_s Angle between the leg axis and the plane containing the shear reinforcement

β_1 Factor relating the depth of the equivalent rectangular compressive stress block to the depth of neutral axis (ACI, 2014, Sect. 22.2.2.4.1)

$\gamma_{f,sls}$ Load partial safety factor for SLS

$\gamma_{f,uls}$ Load partial safety factor for ULS

ϵ Generic strain

$\hat{\epsilon}$ Quantity less than 1

ϵ_c Strain in the concrete

$\epsilon_{c,min}$ Minimum strain in the concrete

$\epsilon_{c,max}$ Max strain in the concrete

ϵ_{cu} Ultimate strain for the concrete, -0.003 (ACI, 2014, Sect.22.2.2.1)

$\epsilon_c(y)$ Strain in the concrete

ϵ_{C1} Strain in cable $C1$

ϵ_{C2} Strain in cable $C2$

$\epsilon_{max,tp}$ Strain in the prestressed tendon

ϵ_{pe} Tensile strain in the tendon at prestress transfer level including relaxation effects

$\epsilon_{p,i}$ Strain in the i-th prestressed tendon

$\hat{\epsilon}_{p,i}$ Contribution to the i-th prestressed tendon strain due to bending in the cross-section

$\epsilon_{p0,i}$ Strain in the i-th prestressed tendon due to prestress only

$\epsilon_p(y)$ Strain in the prestressed tendon

$\epsilon_p(y_{p,i})$ Strain in the prestressed tendon

$\epsilon_{s,i}$ Strain in the i-th rebar

$\epsilon_s(y)$ Strain in the rebar

$\epsilon_s(y_{s,i})$ Strain in the rebar

ϵ_{ty} Strain in the generic reinforcement at yield, if prestressed it is set at 0.002 for ACI (2014)

θ_{crk} Angle between crack and member axis, usually taken as 45 deg

θ_{C1} Angle between global x and cable $C1$

$\theta_{C1,0}$ Angle between global x and cable $C1$ before B is deflected

θ_{C2} Angle between global x and cable $C2$

$\theta_{C2,0}$ Angle between global x and cable $C2$ before B is

deflected

θ_L Angle between global x and leg

$\theta_{L,0}$ Angle between global x and leg before B is deflected

λ Modification factor reflecting the reduced mechanical properties of lightweight concrete

ν Poisson's ratio

ν_c Concrete Poisson's ratio

ν_s Longitudinal reinforcement Poisson's ratio

ν_{st} Shear reinforcement Poisson's ratio

ν_t Cable Poisson's ratio

ρ Material density

ρ_c Concrete density

ρ_{ceff} Effective concrete density

ρ_p Cable density

ρ_s Longitudinal reinforcement density

ρ_{st} Shear reinforcement density

ρ_{stm} Minimum spiral/tie volume ratio (ACI, 2014, Section 10.9.3)

ρ_{stv} Spiral/tie volume ratio (ACI, 2014, Section 10.9.3)

σ_{cz} Normal (axial) stress in the concrete

$\sigma_{cz}(y)$ Normal (axial) stress in the concrete

σ_{C1} Normal (axial) stress in cable set $C1$

σ_{C2} Normal (axial) stress in cable set $C2$ at pre-stressing

σ_{C1pt} Normal (axial) stress in cable set $C1$ at pre-stressing

σ_{C2pt} Normal (axial) stress in cable set $C2$ at pre-stressing

σ_{pz} Normal (axial) stress in the prestressed tendon

$\sigma_{pz}(y_{p,i})$ Normal (axial) stress in the i-th prestressed tendon element

σ_{sz} Normal (axial) stress in the rebar element

$\sigma_{sz}(y_{s,i})$ Normal (axial) stress in the i-th rebar element

ϕ_{ACI} Strength reduction factor (ACI, 2014, Section 21.2.1)

ψ_1 Angle described by the chord of the outer circular segment at coordinate y_a

ψ_2 Angle described by the chord of the inner circular segment at coordinate y_a

D. Extended Beam Theory Development

Starting from the analysis of an infinitesimal beam segment of a leg as shown in Fig. 7, the balance of the forces is written along y_b and z_b in the local (undeformed) coordinate system as in Eq. (43).

$$\begin{cases} (N + dN)\cos\left[v'\left(z_b + dz_b\right)\right] - N\cos\left[v'\left(z_b\right)\right] + T\sin\left[v'\left(z_b\right)\right] - (T + dT)\sin\left[v'\left(z_b + dz_b\right)\right] + p(z_b)dz_b = 0 \\ (T + dT)\cos\left[v'\left(z_b + dz_b\right)\right] - T\cos\left[v'\left(z_b\right)\right] - N\sin\left[v'\left(z_b\right)\right] + (N + dN)\sin\left[v'\left(z_b + dz_b\right)\right] + q(z_b)dz_b = 0 \end{cases}$$

$$(43)$$

where N is the axial load at the span station of interest; v is the deflection normal to beam axis in the y_b direction; T is the shear component along the y-axis at span station of interest; $p(z_b)$ is the component of the external, distributed static loading along the beam z_b axis; $q(z_b)$ is the component of the external, distributed static loading along the beam y_b axis; d denotes the differential operator. The prime symbols $'$, $''$, and $'''$ denote first, second, and third order spatial derivatives relative to z_b, respectively. By adopting the definitions in Eq. (44), one obtains Eq. (4).

$$\begin{aligned} (N + dN) &= N|_{z_b + dz_b} \\ \cos\left[v'\left(z_b + dz_b\right)\right] &= \cos\left(v'\right)|_{z_b + dz_b} \end{aligned}$$

$$(44)$$

$$\begin{cases} d\left(N\cos\left(v'\right)\right) - d\left(T\sin\left(v'\right)\right) + p(z_b)dz_b = 0 \\ d\left(T\cos\left(v'\right)\right) + d\left(N\sin\left(v'\right)\right) + q(z_b)dz_b = 0 \end{cases}$$

$$(\text{4 revisited})$$

Under the hypotheses mentioned in Section 4, Eq. (4) can be integrated from z_b=0 m to z_b to give:

$$\begin{cases} N\cos\left(v'\right) - T\sin\left(v'\right) = c_1 + m_{eff}g\sin\theta_L z_b \\ N\sin\left(v'\right) + T\cos\left(v'\right) = c_2 - m_{eff}g\cos\theta_L z_b \end{cases}$$

$$(45)$$

Among the boundary conditions at z_b=0 m (Fig. 17), one could write the force balance along z_b and y_b in the beam local coordinate system. The reaction at the joint A is divided into two contributions: one aligned with the global Z_G, and one, N_e, with $\overline{AB}$. It is straightforward to verify that the vertical component must be equal to 1/2 the effective

weight of the beam. No other force can act on joint A for equilibrium of the leg. Thus, one arrives at Eq. (46):

$$\begin{cases} N(0)\cos\left(v'(0)\right) - T(0)\sin\left(v'(0)\right) + N_e + \dfrac{m_{eff}\,g\,L_{L0}}{2}\sin\left(v'(0)\right) = 0 \\ N(0)\sin\left(v'(0)\right) + T(0)\cos\left(v'(0)\right) - \dfrac{m_{eff}\,g\,L_{L0}}{2}\cos\left(v'(0)\right) = 0 \end{cases} \tag{46}$$
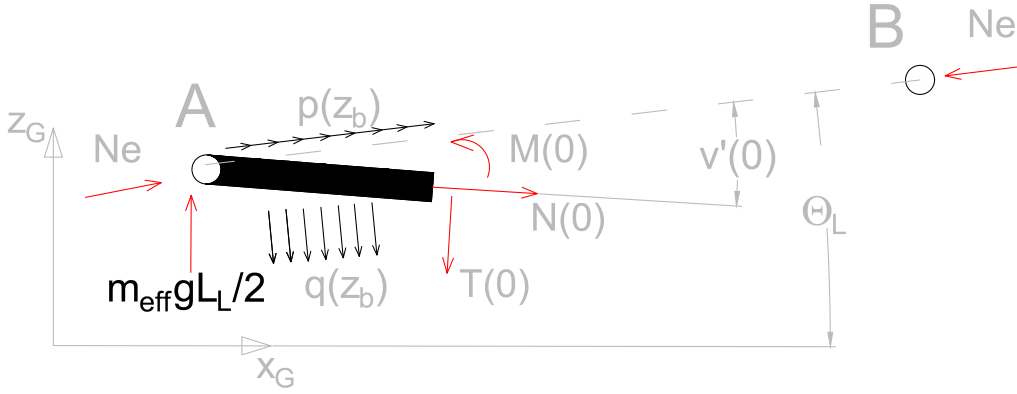

Figure 17: Diagram showing the boundary conditions imposed at $z_b = 0$ m in the development of SOFT4S's structural model. Meaning of symbols in main text.
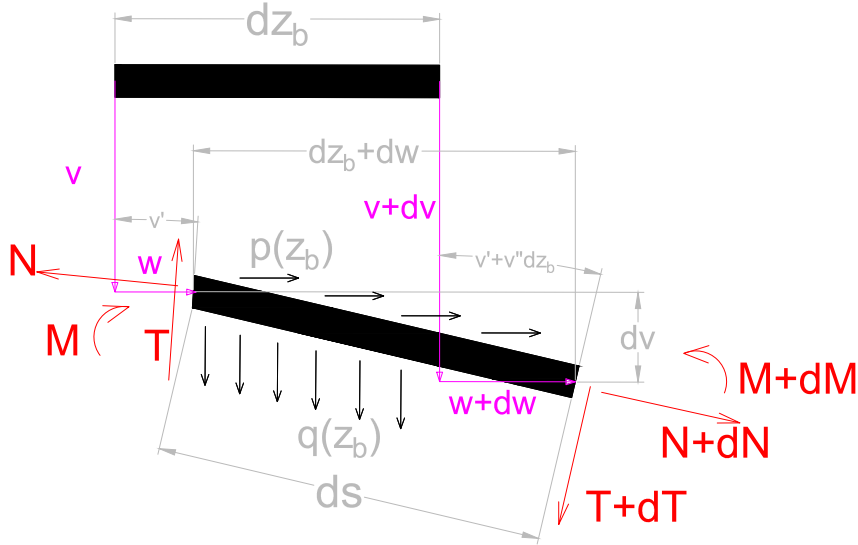

Figure 18: Diagram showing an infinitesimal beam segment undergoing stretching and deflection with applied external and internal forces. Meaning of symbols in main text.

From Eq. (46) and setting $z_b = 0$ in Eq. (45), the integration constants can be calculated as in Eq. (47), and the expressions for N and T can then be obtained as shown in Eq. (6).

$$\begin{cases} c_1 = -N_e - \dfrac{m_{eff}\,g\,L_{L0}}{2}\sin\left(\theta_L\right) \\ c_2 = \dfrac{m_{eff}\,g\,L_{L0}}{2}\cos\left(\theta_L\right) \end{cases} \tag{47}$$

$$\begin{cases} N = -\left[N_e + m_{eff}g\sin\left(\theta_L\right)\left(\frac{L_{L0}}{2} - z_b\right)\right]\cos\left(v'\right) + m_{eff}g\cos\left(\theta_L\right)\left(\frac{L_{L0}}{2} - z_b\right)\sin\left(v'\right) \\ T = \left[N_e + m_{eff}g\sin\left(\theta_L\right)\left(\frac{L_{L0}}{2} - z_b\right)\right]\sin\left(v'\right) + m_{eff}g\cos\left(\theta_L\right)\left(\frac{L_{L0}}{2} - z_b\right)\cos\left(v'\right) \end{cases}$$

(6 revisited)

Turning now to the bending moments, Eq. (48) gives the moment balance about the right end of the beam segment and along the local $x_b \equiv Y_G$ (see also Fig. 18):

$$dM - \left[N\sin\left(v'\right) + T\cos\left(v'\right)\right]\left(dw + dz_b\right) + \left[N\cos\left(v'\right) - T\sin\left(v'\right)\right]dv +$$
$$q(z_b)dz_b\frac{\left[dw + dz_b\right]}{2} - p(z_b)dz_b\frac{dv}{2} = 0$$

(48)

where M is the bending moment about the local x_b axis at the span station of interest. In the limit $dz_b \to 0$, Eq. (48) rewrites as in Eq. (49):

$$M' - \left[N\sin\left(v'\right) + T\cos\left(v'\right)\right]\left(1 + w'\right) + \left[N\cos\left(v'\right) - T\sin\left(v'\right)\right]v' + q(z_b)dz_b\frac{\left[w' + 1\right]}{2} - p(z_b)dz_b\frac{v'}{2} = 0$$

(49)

Eq. (7) derives directly from Eq. (49) for $dz_b \simeq 0$.

$$M' - \left[N\sin\left(v'\right) + T\cos\left(v'\right)\right]\left(1 + w'\right) + \left[N\cos\left(v'\right) - T\sin\left(v'\right)\right]v' = 0$$

(7 revisited)

Making use of Eq. (6), Eq. (7) can rewrite as in Eq. (8):

$$M' = \left[m_{eff}g\cos\left(\theta_L\right)\left(\frac{L_{L0}}{2} - z_b\right)\right]\left(1 + w'\right) + \left[N_e + m_{eff}g\sin\left(\theta_L\right)\left(\frac{L_{L0}}{2} - z_b\right)\right]v'$$

(8 revisited)

At $z_b = 0$ m the following boundary conditions apply:

$$\begin{aligned} v(0) &= 0 \\ w(0) &= 0 \\ M(0) &= 0 \end{aligned}$$

(50)

Integrating Eq. (8) between $z_b = 0$ m and the generic $\hat{z}_b$, and making use of the boundary conditions in Eq. (50) and of the equality (by-parts integration) in Eq. (51), one arrives at the expression for the bending moment about x_b as written in Eq. (52).

$$\int_0^{\hat{z}_b}\left(\frac{L_{L0}}{2} - z_b\right)\frac{df}{dz_b}dz_b = \left(\frac{L_{L0}}{2} - \hat{z}_b\right)f\left(\hat{z}_b\right) - \frac{L_{L0}}{2}f(0) + \int_0^{\hat{z}_b}f\left(z_b\right)dz_b =$$
$$\left(\frac{L_{L0}}{2} - \hat{z}_b\right)f\left(\hat{z}_b\right) - \frac{L_{L0}}{2}f(0) + \hat{z}_b\overline{f}$$

(51)

where the mean value theorem of integrals was used and $\overline{f} = f(z_m)$, with $z_m \in (0, z_b)$ such that $f(z_m) = \frac{1}{\hat{z}_b}\int_0^{\hat{z}_b}f\left(z_b\right)dz_b$;

$$M = N_e v(z_b) + m_{eff}g\sin\left(\theta_L\right)\left[\left(\frac{L_{L0}}{2} - z_b\right)v(z_b) + \overline{v}z_b\right]$$
$$+ m_{eff}g\cos\left(\theta_L\right)\left(\frac{L_{L0}}{2}z_b - \frac{z_b^2}{2}\right) + m_{eff}g\cos\left(\theta_L\right)\left[\left(\frac{L_{L0}}{2} - z_b\right)w(z_b) + \overline{w}z_b\right]$$

(52)

By employing Euler's approximation between moment and beam axis curvature as shown in Section 4.1, a second order, linear ODE can be derived for the deflection v. This ODE does not lend itself to an analytical solution, and in what follows we will perform some simplifications.

The first simplification neglects the terms containing w. In concrete, it is common to assume a maximum compressive strain at ULS $\epsilon_{cu} \simeq -0.003$, thus the term $(1 + w')$ in Eq. (8) can be taken as 1, and the integral equation becomes:

$$E_c J_{xxceff} v'' + N_e v(z_b) + m_{eff} g \sin\left(\theta_L\right) \left[\left(\frac{L_{L0}}{2} - z_b\right) v(z_b) + \bar{v} z_b\right] + m_{eff} g \cos\left(\theta_L\right) \left(\frac{L_{L0}}{2} z_b - \frac{z_b{}^2}{2}\right)$$

(53)

Eq. (53) contains the boundary condition $M(0) = 0$, but it is instructive to use the zero-moment condition at $z_b = L_{L0}$:

$$0 = M(L_{L0}) = N_e v(L_{L0}) + m_{eff} g \sin\left(\theta_L\right) L_{L0} \left[\bar{v} - \frac{v(L_{L0})}{2}\right]$$

(54)

In the case of a flexural rigid beam, the term in brackets vanishes (hint, in a rigid rotation the deflection normal to the beam axis is linear in z_b), and the conditions translates into having $v(L_{L0}) = 0$. Note that, in general, we cannot a-priori set this boundary conditions for a non-rigid beam.

Eq. (53) is an ODE of the second order with variable coefficients, which does not have a readily useful analytical solution.

The second simplification we carry out in the differential form of Eq. (8) is to replace the term $m_{eff} g \sin\left(\theta_L\right) \left(\frac{L_{L0}}{2} - z_b\right)$ that multiplies v' with its mean value in $(0, L_{L0})$, which can be easily proven to be 0. With this final approximation, we obtain:

$$E_c J_{xxceff} v''' + N_e v'(z_b) + m_{eff} g \cos\left(\theta_L\right) \left(\frac{L_{L0}}{2} - z_b\right) = 0$$

(55)

The solution to Eq. (55) is given by Eq. (56) as the sum of the generic solution to the homogeneous equation as in Eq. (57), and the particular solution as in Eq. (58):

$$v(z_b) = v_h(z_b) + v_p(z_b)$$

(56)

$$v_h(z_b) = \bar{a} + \left(a_c \cos(\alpha z_b) + b_c \sin(\alpha z_b)\right)$$

(57)

$$v_p(z_b) = c_1 - \frac{m_{eff} g}{N_e} \left(\frac{L_{L0}}{2} z_b - \frac{z_b{}^2}{2}\right) \cos(\theta_L)$$

(58)

$$\text{where} \quad \alpha = \sqrt{\frac{N_e}{E_c J_{xxceff}}}$$

(59)

By applying the boundary conditions shown in Eq. (60), one can find the expressions for the constants $\bar{\bar{a}} = c_1 + \bar{a}$, a_c, b_c to return an expression for v as in Eq. (9).

$$\begin{cases} v(0) & = & 0 \\ v''(0) & = & 0 \\ v''(L_{L0}) & = & 0 \end{cases}$$

(60)

$$v(z_b) = \frac{m_{eff} g}{N_e \alpha^2} \cos(\theta_L) \left[\cos(\alpha z_b) + \frac{1 - \cos(\alpha L_{L0})}{\sin(\alpha L_{L0})} \sin(\alpha z_b) - \frac{L_{L0} - z_b}{2} z_b \alpha^2 - 1\right]$$

(9 revisited)

D.1. Compatibility Equation and Solution of the Structural System

From an analysis of Fig. 18, one can write:

$$\begin{aligned} ds &= \sqrt{(v' dz_b)^2 + (w' dz_b + dz_b)^2} = \\ & dz_b \sqrt{v'^2 + w'^2 + 2w' + 1} = \\ & dz_b \sqrt{v'^2 + (1 + w')^2} \end{aligned}$$

(61)

For $(1 + w') \simeq 1$, this leads to the beam strain component associated with shortening due to bending:

$$\epsilon = \frac{ds - dz_b}{dz_b} = \sqrt{1 + v'^2} - 1 \simeq \frac{1}{2} v'^2 \tag{62}$$

where in Eq. (62), a Taylor expansion up to the first order was used for $v' \rightarrow 0$.

If, however, we consider the quantity $\hat{\epsilon} = v'^2 + w'^2 + 2w' << 1$, and expand Eq. (61) in a Taylor series retaining terms up to the second order, we can write:

$$\epsilon = \frac{ds - dz_b}{dz_b} \simeq \frac{1}{2} \left[v'^2 + w'^2 + 2w' \right] - \frac{1}{8} \left[v'^2 + w'^2 + 2w' \right]^2 + o(2) \simeq \\ \frac{1}{2} v'^2 + w' + o(2) \tag{63}$$

Thus the total strain ϵ is given by the sum of axial strain, w', and the shortening of the beam due to bending, $\frac{1}{2} v'^2$, and a second-order constitutive equation can be attained:

$$N = E_c A_{Leff} \epsilon = E_c A_{Leff} \left[\frac{1}{2} v'^2 + w' \right] \tag{12 revisited}$$

Starting from Eq. (6), and acknowledging Eq. (12), one can write a PDE for w that includes terms in v:

$$E_c A_{Leff} w' = - \left[N_e + m_{eff} g \sin \left(\theta_L \right) \left(\frac{L_{L0}}{2} - z_b \right) \right] \cos \left(v' \right) \\ + m_{eff} g \cos \left(\theta_L \right) \left(\frac{L_{L0}}{2} - z_b \right) \sin \left(v' \right) - E_c A_{Leff} \frac{1}{2} v'^2 \tag{64}$$

For small angle deflections, ($v' << 1$, hence $\cos(v') \simeq 1$, and $\sin(v') \simeq v'$), Eq. (64) can be simplified as in Eq. (65):

$$E_c A_{Leff} w' = - \left[N_e + m_{eff} g \sin \left(\theta_L \right) \left(\frac{L_{L0}}{2} - z_b \right) \right] + m_{eff} g \cos \left(\theta_L \right) \left(\frac{L_{L0}}{2} - z_b \right) v' - E_c A_{Leff} \frac{1}{2} v'^2 \tag{65}$$

and by replacing v with the expression in (9), Eq. (66) is attained.

$$w' = -\frac{1}{E_c A_{Leff}} \left[N_e + m_{eff} g \sin \left(\theta_L \right) \left(\frac{L_{L0}}{2} - z_b \right) \right] \\ + \frac{\left(m_{eff} g \cos(\theta_L) \right)^2}{E_c A_{Leff} N_e \alpha} \left(\frac{L_{L0}}{2} - z_b \right) \left[-\sin(\alpha z_b) - \frac{\alpha}{2} \left(L_{L0} - 2 z_b \right) + \frac{1 - \cos(\alpha L_{L0})}{\sin(\alpha L_{L0})} \cos(\alpha z_b) \right] \\ - \frac{\left(m_{eff} g \cos(\theta_L) \right)^2}{2 N_e^2 \alpha^2} \left[-\sin(\alpha z_b) - \frac{\alpha}{2} \left(L_{L0} - 2 z_b \right) + \frac{1 - \cos(\alpha L_{L0})}{\sin(\alpha L_{L0})} \cos(\alpha z_b) \right]^2 \tag{66}$$

By integrating Eq. (66) with the boundary conditions in Eq. (50), the expression for $w(z_b)$ can be reached as in Eq. (13).

$$
\begin{aligned}
w(z_b) = &-\frac{1}{E_c A_{Leff}} \left[N_e * z_b + m_{eff} g \sin\left(\theta_L\right) \left(\frac{L_{L0} z_b - z_b^2}{2} \right) \right] \\
&+ \frac{\left(m_{eff} g \cos(\theta_L)\right)^2}{E_c A_{Leff} N_e} \left[\frac{1}{\alpha^2} \left(\frac{L_{L0}}{2} - z_b \right) \cos\left(\alpha z_b\right) - \frac{L_{L0}}{2\alpha^2} + \frac{\sin\left(\alpha z_b\right)}{\alpha^3} \right. \\
&+ \frac{6 L_{L0} z_b^2 - 3 L_{L0}^2 z_b - 4 z_b^3}{12} + \tan\frac{\alpha L_{L0}}{2} \left(\frac{\sin(\alpha z_b)}{\alpha^2} \left(\frac{L_{L0}}{2} - z_b \right) + \frac{1}{\alpha^3} \left(1 - \cos\left(\alpha z_b\right)\right) \right) \Bigg] \\
&+ \frac{\left(m_{eff} g \cos(\theta_L)\right)^2}{2 N_e^2 \alpha^3} \left[-\frac{\alpha z_b}{2} + \frac{\sin\left(2\alpha z_b\right)}{4} + \frac{-4 z_b^3 + 6 L_{L0} z_b^2 - 3 L_{L0}^2 z_b}{12} \alpha^3 \right. \\
&- \tan^2\frac{\alpha L_{L0}}{2} \left(\frac{\alpha z_b}{2} + \frac{\sin\left(2\alpha z_b\right)}{4} \right) + 2\sin\left(\alpha z_b\right) - \alpha L_{L0} + \alpha\left(L_{L0} - 2 z_b\right)\cos\left(\alpha z_b\right) \\
&+ \tan\frac{\alpha L_{L0}}{2} \left(1 - \cos^2\left(\alpha z_b\right)\right) + \tan\frac{\alpha L_{L0}}{2} \left(2 - 2\cos\left(\alpha z_b\right) + \alpha(L_{L0} - 2 z_b)\sin(\alpha z_b)\right) \Bigg]
\end{aligned}
$$

$$\text{(13 revisited)}$$

By calculating $w(L_{L0})$, the compatibility equation required to solve the indeterminate system of equations in Eq. (1) is written as in Eq. (16). Through some algebraic and trigonometric reductions, and by recognizing that $w(L_{L0}) = L_L - L_{L0}$, Eq. (16) rewrites as in Eq. (67):

$$
\begin{aligned}
\frac{E_c A_{Leff}(L_L - L_{L0})}{L_{L0}} = &-N_e - \frac{\left(m_{eff} g \cos(\theta_L)\right)^2}{12 E_c J_{xxceff}} L_{L0}^4 \left[\frac{1}{L_{L0}^2 \alpha^2} + \frac{12}{L_{L0}^4 \alpha^4} - \frac{24}{L_{L0}^5 \alpha^5} \tan\frac{\alpha L_{L0}}{2} \right] \\
&- E_c A_{Leff} \frac{\left(m_{eff} g \cos(\theta_L)\right)^2}{24 E_c^2 J_{xxceff}^2} L_{L0}^6 \left[\frac{1}{\alpha^4 L_{L0}^4} - \frac{60}{L_{L0}^7 \alpha^7} \tan\frac{\alpha L_{L0}}{2} \right. \\
&\left. + \frac{24}{\alpha^6 L_{L0}^6} + \frac{12\left(1 - \cos(\alpha L_{L0})\right)}{\alpha^6 L_{L0}^6 \sin^2\left(\alpha L_{L0}\right)} \right]
\end{aligned}
$$

$$\text{(67)}$$

where L_L is a function of θ_L, i.e., the final angle assumed by the line connecting $\overline{AB}$.

The system of equations to solve for the axial loads can finally be written as in Eq. (17).

If the final configuration angles (θ_{C1}, θ_{C2}, θ_L) and the final length of the leg L_L are known, then Eq. (17) can be solved for the unknowns N_{C1}, N_{C2}, and N_e. However, it is unlikely that these quantities would be known a-priori, unless a fixed geometry is desired. It is more useful to express the angles of the components and the final length of the leg in terms of global displacements of the hinge at B, i.e., (u_B, w_B) as in Eq. (18) and Eq. (19).

E. Service Limit State Verification Criteria

To verify the structure against SLS, the following criteria[3] must be met. Some of these criteria allow the stress linear treatment of Section 5.1.1 to be applicable within an inhomogenous cross-section. The torsion load is expected to be negligible, given the moment free connection joint with the buoyancy can, thereby items 12-13 are shown only for completeness.

1. Ensure cross-sectional properties are similar in any direction, i.e., impose minimum number of longitudinal reinforcement: $n_{s,i}, n_{s,o} \geq 8$; where $n_{s,i}$ and $n_{s,o}$ are the numbers of inner and outer longitudinal reiforcement, respectively.

2. Ensure minimum concrete cover (e.g., 3 in, given the harsh and corrosive marine environment) on outer (near the outer surface) and inner (near the inner surface) reinforcement elements: $\dfrac{D_L - (D_{s,o} + d_{s,o} + 2d_{sso})}{2} >$

---

[3] The meaning of symbols used in these criteria is further given in Table 1 and in Appendices B–C.

1.5 in..3 in and $\dfrac{(D_{s,i} - d_{s,i} - 2d_{ssi}) - d_L}{2} > 1.5$ in..3 in.

3. Ensure distance among longitudinal reinforcement elements is within allowables (e.g., minimum clear spacing

   ACI, 2014, Sections 7.6.7.1 and 25.2): $\begin{cases} \dfrac{\pi D_{s,i}}{n_{s,i}} - d_{s,i} > \max\left(1.5\,\text{in}, 1.5d_{s,i}\right) \\ \dfrac{\pi D_{s,o}}{n_{s,o}} - d_{s,o} > \max\left(1.5\,\text{in}, 1.5d_{s,o}\right) \end{cases}$.

4. Verify that the maximum compressive strain is below allowable: $\epsilon_{c,min} > -0.003$.

5. Verify that the maximum compressive stresses in the concrete lie below a safe threshold (also minimizing fatigue failure risk) (ACI, 2014, Sections 24.5.3.2 and 24.5.4.1): $\min\left(\sigma_{cz}\right)\gamma_{f,sls} > -0.85f_c\phi_{ACI} \simeq -0.6f_c$; ϕ_{ACI} is the strength reduction factor (ACI, 2014, Section 21.2.1).

6. Ensure the section is uncracked: $\epsilon_c(D_L/2) \le 0$.

7. Ensure the maximum rebar stress is below the allowable values: $|\gamma_{f,sls} \max_i \left(\sigma_{sz}(y_{s,i})\right)| \le \phi_{ACI}f_{ys}$, where f_{ys} is the longitudinal reinforcement yield strength.

8. Ensure maximum cable stress below allowable: $\gamma_{f,sls} \max\left(\sigma_{C1}, \sigma_{C2}\right) \le \phi_{ACI}f_{yc}$, where f_{yc} is the cable yield strength.

9. Ensure a minimum quantity (A_{stot}) of longitudinal reinforcement for flexural members:

   A_{stot}: $A_{stot} > \max\left(200\dfrac{(D_L - d_L)0.8D_L}{f_{ys}}, 3 * \sqrt{f_c}\dfrac{(D_L - d_L)0.8D_L}{f_{ys}}\right)$ in imperial units (ACI, 2014, Section 9.6.1.2);

   A_{stot}: $0.01 < \dfrac{A_{stot}}{A_g} \le 0.08$ (ACI, 2014, Section 10.6);

   A_{stot}: $A_{stot} \ge 0.004A_{ct}$, where A_{ct} is the area of that part of the cross section between the flexural tension face and the centroid of the gross section, (ACI, 2014, Section 9.6.2.3).

10. Ensure minimum quantity of shear reinforcement: $\dfrac{A_v + 2A_{st}}{s_{sv}} \ge \max\left(0.75\sqrt{f_c}\dfrac{D_L - d_L}{f_{yst}}; 50\dfrac{D_L - d_L}{f_{yst}}\right)$ in imperial units (ACI, 2014, Sec.s 9.6.3.3, 9.6.4.2, and 10.6.2.2); where A_v is the torsional shear reinforcement (spiral/tie) cross-sectional area; A_{st} is the shear reinforcement (spiral/tie) cross-sectional area; and s_{sv} is the shear reinforcement (spiral/tie) spacing; f_{yst} is the stirrup/tie yield strength.

11. Ensure spacing of shear reinforcement is less than maximum values (ACI, 2014, Sections 10.7.6.5 and 25.7.2.1) given by:

$$s_{sv} \le \left[\begin{cases} \min\left(24\,\text{in}; 3h_b/4\right) & \text{if} \quad V_s \le 4\sqrt{f_c}(D_L - d_L)0.8D_L \\ \min\left(12\,\text{in}; 3h_b/8\right) & \text{if} \quad V_s > 4\sqrt{f_c}(D_L - d_L)0.8D_L \end{cases}, \min\left(48d_{sso}, 16d_{s,o}, 0.75D_L, 24\,\text{in}\right)\right] \tag{68}$$

where all the quantities are in inches, pound force, and psi; where h_b is the height/depth of the cross-section; V_s is the shear strength due to tie/spiral reinforcement. The contribution to the nominal shear strength of the cross-section (V_n) due to the shear reinforcement (V_s) and the concrete (V_c) are given by ACI (2014, Section 22.5.1.2, 22.5.5-22.5.7):

$$V_n = \phi_{ACI}\left(V_s + V_c\right) \tag{69}$$

with $\quad V_s = \min\left(A_{vtot}f_{yst}\dfrac{d_{sh}}{s_{st}} * (\cos\alpha_s + \sin\alpha_s), 8\sqrt{f_c}\left(D_L - d_L\right)d_{sh}\right) \tag{70}$

$$\text{and} \quad V_c = \begin{cases} 2\left(1 - \dfrac{N}{2000A_g}\right)\lambda * \sqrt{f_c}\left(D_L - d_L\right)d_{sh} & \text{if} \quad N < 0. \\[2ex] 2\lambda * \sqrt{f_c}\left(D_L - d_L\right)d_{sh} & \text{if} \quad N = 0. \\[2ex] 2\left(1 - \dfrac{N_u}{500A_g}\right)\lambda * \sqrt{f_c}\left(D_L - d_L\right)d_{sh} & \text{if} \quad N > 0. \end{cases} \tag{71}$$

where ϕ_{ACI}=0.75 for shear and torsion verifications; d_{sh} is the distance to the center of pre and non-prestressed tension reinforcement from top fiber, but $\leq 0.8h_b$, taken as $d_{sh} = 0.8D_L$; and α_s is the angle between the leg axis and the plane containing the shear reinforcement.

12. Ensure that stirrup/tie/spiral spacing is adequate for torsion per ACI (2014, Section 11.5.6.1):

$$\begin{cases} s_{sv} & < & \dfrac{p_h}{8} \\[2ex] s_{sv} & < & 12\,\text{in} \end{cases} \tag{72}$$

where s_{sv} is the shear reinforcement (spiral/tie) spacing; p_h is the perimeter described by centerline of stirrup element.

13. Ensure that extra longitudinal reinforcement exists and is above minimum for torsion per (ACI, 2014, Section 9.6.4.3):

$$A_l \geq \min\left(5\sqrt{f_c}\dfrac{A_{cp}}{f_{yst}} - A_{st}s_{sv}p_h\dfrac{f_{yst}}{f_{yl}}\right), \dfrac{5A_{cp}\sqrt{f_c}}{f\,yl}s_{sv} - \dfrac{25(D_L - d_L)}{f_{yst}}p_h\dfrac{f_{yst}}{f_{yl}} \tag{73}$$

where A_{cp} is the area enclosed by outside perimeter of concrete cross section; f_{yl} is the torsional longitudinal reinforcement yield strength; A_l is the torsional additional longitudinal reinforcement total cross-sectional area. A_l can be the total longitudinal reinforcement area used minus the one needed to satisfy all the other criteria above for flexural and compression, and must be uniformly distributed around the cross-section at 12 in spacing or less.

F. Ultimate Limit State Verification Criteria

To verify the structure against ULS, the following criteria must be met:

1. Ensure maximum utilizations for normal force and bending moments (left-hand sides of Eq. (74)) are less than unity:

$$\begin{aligned} \dfrac{\gamma_{f,uls}N}{\phi_{ACI}P_n^*} &\leq 1 \\[2ex] \dfrac{\gamma_{f,uls}M}{\phi_{ACI}M_n} &\leq 1 \end{aligned} \tag{74}$$

In Eq. (74), P_n^* is the nominal axial strength, in either tension or compression depending on the N sign per Eq.s (41)-(42). The utilizations can be checked by ensuring there is sufficient horizontal ($\phi_{ACI}M_n$ - $\gamma_{f,uls}M$ for the given N_u) and vertical ($\phi_{ACI}P_n$ - $\gamma_{f,uls}N$ for the given M_u) margin between the factored external loads and the safe limit curve of the interaction diagram.

2. Ensure maximum rebar stress below allowable: $\gamma_{f,uls}\max_i\left(\sigma_{sz}(y_{s,i})\right) \leq \phi_{ACI}f_{us}$; where f_{us} is the longitudinal reinforcement ultimate strength;

3. Ensure maximum tendon stress below allowable: $\gamma_{f,uls}\max_i\left(\sigma_{pz}(y_{p,i})\right) \leq \phi_{ACI}f_{up}$; where f_{up} is the prestressing tendon ultimate strength;

4. Ensure $1.2M_{cr} < \phi_{ACI}M_u$ per ACI (2014, Section 18.8.2). This condition implies that the total amount of bonded, prestressed and nonprestressed, longitudinal reinforcement shall be adequate to develop a factored load at least 1.2 times the cracking load computed on the basis of the modulus of rupture f_r specified in ACI (2014, Section 9.5.2.3) :

$$M_{cr} = \dfrac{f_r J_{xxg}}{D_L/2} \tag{75}$$

$$f_r = 7.5\lambda\sqrt{f_c} \tag{76}$$

where J_{xxg} denotes the gross cross-sectional second area moment of inertia.

5. Ensure adequate shear strength: $\gamma_{f,uls} * T \le V_n$ (see Eq.s (69)–(71));

6. Ensure adequate cross-section size against torsion (avoid cracking) (ACI, 2014, Section 22.7.7):

$$\frac{\gamma_{f,uls}T}{(D_L - d_L)\,d_{sh}} + \frac{\gamma_{f,uls}M_z p_h}{1.7 A_{oh} t_w} \le \phi_{ACI}\left(\frac{V_c}{(D_L - d_L)\,d_{sh}} + 8\sqrt{f_c}\right) \quad \text{if} \quad t_w < \frac{A_{oh}}{p_h} \tag{77}$$

$$\frac{\gamma_{f,uls}T}{(D_L - d_L)\,d_{sh}} + \frac{\gamma_{f,uls}M_z p_h}{1.7 A_{oh}{}^2} \le \phi_{ACI}\left(\frac{V_c}{(D_L - d_L)\,d_{sh}} + 8\sqrt{f_c}\right) \quad \text{otherwise} \tag{78}$$

where $\gamma_{f,uls}T$ is the *factored* shear component along the y-axis at span station of interest; p_h is the perimeter described by centerline of stirrup element; A_{oh} is the area enclosed by centerline of shear (spiral/tie) reinforcement; t_w is the wall thickness; $\gamma_{f,uls}M_z$ is the *factored* torque at the span station of interest; ϕ_{ACI}=0.75 for shear and torsion verifications.

7. Ensure adequate torsional strength: $M_{zu}=\gamma_{f,uls}M_z \le T_{qn}$ (ACI, 2014, Section 22.7.6.1):

$$T_{qn} = 2A_o A_{st} \frac{f_{yst}}{s_{sv}\tan(\theta_{crk})}\phi_{ACI} \tag{79}$$

where T_{qn} is the nominal torsional strength; A_o is the area enclosed by the shear (spiral/tie) flow path; A_{st} is the shear reinforcement (spiral/tie) cross-sectional area; s_{sv} is the shear reinforcement (spiral/tie) spacing; θ_{crk} is the angle between crack and member axis, usually taken as 45 deg.

Acknowledgments

CRediT authorship contribution statement

Rick Damiani: Conceptualization of this study, Methodology, Software, Original draft preparation. **Max Franchi:** Conceptualization of this study, Methodology.

References

ACI, 2014. 318-14 - building code requirements for structural concrete and commentary.

Allen, H.L., 2019. Global performance testing, simulation, and optimization of a 6-mw annular floating offshore wind turbinehull.

Banister, K., 2018. Floating offshore wind: Projects and prospects, in: Ocean Renewable Energy Conference. URL: https://pacificoceanenergy.org/wp-content/uploads/2018/09/OREC-2018_Presentation_Kevin-Bannister.pdf.

Choisnet, T., Geshier, B., Vetrano, G., 2016. Initial comparison of concrete and steel hulls in the case of Ideol's square ring floating substructure, in: The 15th World Wind Energy Conference, Tokyo, Japan.

DNV-GL, 2018. DNVGL-ST-0126 – support structures for wind turbines.

Dykes, K., Meadows, R., Felker, F., Graf, P., Hand, M., Lunacek, M., Michalakes, J., Moriarty, P., Musial, W., Veers, P., 2011. Applications of Systems Engineering to the Research, Design, and Development of Wind Energy Systems. Technical Report NREL/TP-5000-52616. NREL. Golden, Colorado.

ECS, 2004. Eurocode 2: Design of concrete structures.

FIB, 2013. Model code for concrete structures 2010. 434 pp.

Gilbert, R.I., Mickleborough, N., 2004. Design of Prestressed Concrete. CRC Press. 528 pp.

Gray, J.S., Hwang, J.T., Martins, J.R.R.A., Moore, K.T., Naylor, B.A., 2019. OpenMDAO: An open-source framework for multidisciplinary design, analysis, and optimization. Structural and Multidisciplinary Optimization 59, 1075–1104. doi:10.1007/s00158-019-02211-z.

IEC, 2019. IEC TS 61400-3-2:2019 wind energy generation systems - part 3-2: Design requirements for floating offshore wind turbines.

Jonkman, J., 2013. New modularization framework for the FAST wind turbine CAE tool, in: Proceedings of the 51st AIAA Aerospace Sciences Meeting, AIAA, Dallas, TX.

MacGregor, J.G., 2011. Reinforced Concrete: Mechanics and Design. Prentice Hall. 1176 pp.

Musial, W., Beiter, P., Schwabe, P., Tian, T., Stehly, T., Spitsen, P., Robertson, A., Gevorgian, V., 2016a. 2016 Offshore Wind Technologies Market Report. Technical Report NREL/TP-5000-68587; DOE/GO-102017-5031. National Renewable Energy Laboratory. URL: https://www.osti.gov/servlets/purl/1375395.

Musial, W., Heimiller, D., Beiter, P., Scott, G., Draxl, C., 2016b. 2016 Offshore Wind Energy Resource Assessment for the United States. Technical Report NREL-TP-5000-66599. NREL. Golden, CO. URL: http://www.nrel.gov/docs/fy16osti/66599.pdf.

Orcina Ltd, 2020. Orcaflex. URL: https://www.orcina.com/orcaflex/.

Powell, G.H., 2010. Modeling for Structural Analysis — Behavior and Basics. Computers and Structures, Inc., Berkley, CA.

Stehly, T., Beiter, P., 2019. 2018 cost of wind energy review. URL: https://www.nrel.gov/docs/fy20osti/74598.pdf.

Timoshenko, S., Gere, J., 1963. Theory of Elastic Stability. second ed., McGraw-Hill.

Timoshenko, S., Young, D., 1965. Theory of Structures. Engineering societies monographs. second ed., McGraw-Hill, New York, USA. 567 pp.

Whitney, C., 1937. Design of reinforced concrete members under flexure and combinedflexure and direct compression , 483–498.

Wilson, E.L., 2002. Three Dimensional Static and Dynamic Analysis of Structures. 3 ed., Computers and Structures, Inc., Berkley, CA.